

Determination of the irreducible representations at high symmetry points of two-dimensional square lattice plasmonic crystals by far-field radiations

T.H. Chan, Y.H. Guan, C. Liu, and H.C. Ong^{a)}

Department of Physics, The Chinese University of Hong Kong, Shatin, Hong Kong, People's Republic of China

As the knowledge of the eigenmode symmetries at high symmetry points (HSPs) in the Brillouin zone is essential in studying the topological properties of electronic and electromagnetic systems, how one can acquire it precisely has become a subject of interest. Here, we employ temporal coupled mode theory (CMT) to determine the irreducible representations of the energy bands at the HSPs in 2D square lattice photonic systems. Our CMT on plasmonic nanohole arrays formulates how Bloch-like surface plasmon polaritons (SPPs) interact not only with each other and but also with the continuum, revealing the importance of mode coupling in defining the field symmetries as well as their radiative and nonradiative characteristics. Such formulation facilitates the assignments of the band representations. From the representations, we find, unlike the conventional 2D tight-binding model, several band inversions occur at the Γ and X points as hole size increases, leading to changes in band topology in a subtle manner. In addition, the radiations arising from the coupled SPPs that carry different field symmetries are strongly polarization- and phase-dependent. We then conduct angle- and polarization-resolved diffraction spectroscopy on plasmonic arrays to verify the theory. Our study paves a simple way toward the probing of the band topology of non-Hermitian systems via far-field.

^{a)} hcong@phy.cuhk.edu.hk

I. INTRODUCTION

In recent years, topology has gone far beyond a mathematical concept and on to become a vital tool in studying condensed matter physics [1], mechanics [2,3], electromagnetism [4,5] and even electronics [6,7], giving rise to several major topics known as topological insulator [1,8-10], acoustics [11-13], and photonics [14-16]. All of them share a common feature that a topologically protected surface or interface state is formed at the boundary between two topological trivial and nontrivial systems [1-16]. Such state is very robust against disorder and perturbation, making it a desirable candidate for making electronic, acoustic, and photonic devices immune to unwanted backscattering. In photonics, various low and high order topological protected states have been demonstrated by using photonic and plasmonic crystals (PhCs and PmCs) spanning from visible to microwave regime [14-21].

The topological triviality of an electromagnetic system is determined by the topologies of the energy bands below the band gap of interest. For example, for one-dimensional (1D) photonic system following Su-Schrieffer-Heeger (SSH) model, the topology of a single band is defined by Zak phase, which is quantized as 0 or π provided the system satisfies inversion symmetry [21-27]. Thus, for any band gap, the summation of all the Zak phases of the bands below it will result in even (including zero) or odd π Zak phases for trivial or nontrivial system [28]. A zero-dimensional (0D) interface state will emerge within the gap when trivial and nontrivial systems are brought together. Several theoretical and experimental studies have been reported on the calculation and the measurement of Zak phase and the formation of the interface states in PhCs and PmCs [21-26]. It also has been shown that, instead of using the Wilson loop method that integrates the Berry connection across the Brillouin zone, Zak phase can be determined simply by examining the symmetries of the eigenmodes at high symmetry points (HSPs) along a continuous energy band [25,26,29]. Same and different symmetries at the Γ

and X points indicate 0 and π Zak phase [26]. For leaky systems, such symmetries are featured as bright and dark modes, providing a simple way to characterize them by far-field [29].

The SSH model has been generalized to higher dimension. Square lattice is a good example of two-dimensional (2D) SSH model. Liu and Wakabayashi have shown for 2D square lattices that support both time-reversal and inversion symmetries, although the Berry curvature is zero, thus zero Chern number, they still exhibit nontrivial topological phase by considering 2D vectorial Zak phase in the Brillouin zone [30,31]. A system with (π, π) Zak phase, which is featured by the band inversions at the X and Y points while those at the Γ and M points remain unchanged, is defined as topological nontrivial and 1D edge state and even higher order 0D corner state can be realized accordingly [32,33]. Generalization to more realistic 2D photonic and acoustic systems have also been reported recently [31,34-38].

As a result, the knowledge of the field symmetries at HSPs is of great importance in determining the topology of a single isolated band or multiple degenerate bands. In fact, Bernevig and his coworkers have developed the so-called topological quantum chemistry (TQC) to study the band topology based on the eigenmode symmetries at HSPs [39]. The symmetries can be used to construct the band representations, which associate with a set of Wannier functions for identifying whether the band topology is trivial, topological, fragile or obstructed atomic limit [40-44]. As the field symmetries can be accessed experimentally, this approach is simpler than the Wilson loop method, which is very computational demanding and experimentally challenging. In addition, since PhCs and PmCs are radiative, the information of the eigenmodes is embedded in the amplitudes and phases of the radiation patterns [29,44-46]. Therefore, one may extract the symmetries of the eigenmodes simply by characterizing the intensities and polarizations of the diffraction orders arising from them.

In this work, we use temporal coupled mode theory (CMT) to study the irreducible representations of the energy bands at the HSPs in 2D square lattice PmCs. CMT shows the

near-fields and the far-field diffraction orders arising from the plasmonic modes are strongly correlated, and they carry the symmetry information [29]. We can properly assign the band representations by performing angle- and polarization-resolved diffraction spectroscopy. For the PmCs we study here, the results agree well with electrodynamic simulations using finite-difference time-domain (FDTD) method, showing the modes at the Γ and X points undergo several subtle band inversions, which are distinctive from the conventional tight-binding SSH model [30,31]. We then fabricate several nanohole PmCs with different hole sizes to verify the theory. Our study proposes a simple method for identifying the irreducible representations and studying the topological properties of lossy and leaky photonic systems.

II. TEMPORAL COUPLED MODE THEORY

We consider an optically thick 2D square lattice PmC and it supports Bloch-like surface plasmon polariton (SPP) modes in which their dispersion relations can be formulated by using the phase-matching equation given as

$$\vec{k}_{SPP} = \left(\frac{2\pi}{\lambda} \sin \theta \cos \varphi + \frac{n_x 2\pi}{P} \right) \hat{x} + \left(\frac{2\pi}{\lambda} \sin \theta \sin \varphi + \frac{n_y 2\pi}{P} \right) \hat{y} \quad \text{in Fig. 1(a), where } \theta \text{ is the}$$

incident polar angle, φ is the azimuthal angle defined with respect to the Γ -X direction, λ is the wavelength, P is the period of the lattice, \vec{k}_{SPP} is the propagation vector of SPP mode, and (n_x, n_y) are the indices specifying the Bragg scattering order [48]. The SPP propagation

constant $|\vec{k}_{SPP}| = \frac{2\pi}{\lambda} \sqrt{\frac{\epsilon_{Au}}{1 + \epsilon_{Au}}}$, where ϵ_{Au} is the dielectric constant of gold. Several dispersive

SPP modes are plotted and labeled with $(0,0)$, $(\pm 1,0)$, $(0,\pm 1)$, and $(-1,\pm 1)$ scattering orders. The grey area is the light cone, showing only the modes that are above it can be excited by far-field. We expect energy band gaps will emerge at the HSPs due to mode coupling [49]. For example, the lowest energy gap at the Γ point, indicated by the red dash box, is formed by the coupling between $(\pm 1,0)$ and $(0,\pm 1)$ SPPs, the second lowest gap at the X point, indicated by the blue

dash box, is due to the coupling between $(0,\pm 1)$ and $(-1,\pm 1)$ SPPs, and finally the lowest gap at the M point results from the coupling between $(0,0)$, $(-1,0)$, $(0,-1)$, and $(-1,-1)$ SPPs. While the gaps at the Γ and X are above the light cone, the gap at the M point is below it. As a result, the SPP modes at the Γ and X gaps are accessible by far-field measurement but not the modes at the M gap, which are near-field excited. In the following, we will focus on the Γ and X points and show the radiation characteristics of the SPP modes can reveal the irreducible representations directly by CMT.

At Γ point

At the Γ point where $\theta = 0^\circ$, the four propagating $(\pm 1,0)$ and $(0,\pm 1)$ SPPs are illustrated in Fig. 1(b), showing they propagate in the $\pm x$ and $\pm y$ directions deduced by the phase-matching equation with $|\vec{k}_{SPP}| = 2\pi/P$. The CMT equation, which has the general form of

$\frac{dA}{dt} = iHA + KS_+$, can be expressed as [29,50-52]:

$$\frac{d}{dt} \begin{bmatrix} a_1 \\ a_2 \\ a_3 \\ a_4 \end{bmatrix} = i \begin{bmatrix} \tilde{\omega}_o & \alpha & \beta & \beta \\ \alpha & \tilde{\omega}_o & \beta & \beta \\ \beta & \beta & \tilde{\omega}_o & \alpha \\ \beta & \beta & \alpha & \tilde{\omega}_o \end{bmatrix} \begin{bmatrix} a_1 \\ a_2 \\ a_3 \\ a_4 \end{bmatrix} + \begin{bmatrix} \kappa & 0 \\ -\kappa & 0 \\ 0 & \kappa \\ 0 & -\kappa \end{bmatrix} \begin{bmatrix} s_{p+} \\ s_{s+} \end{bmatrix}, \quad (1)$$

where a_{1-4} are the mode amplitudes, $\tilde{\omega}_o = \omega_o + i(\Gamma_a + \Gamma_r)/2$ is the complex angular frequency in which Γ_a and Γ_r are the absorption and radiative decay rates considering SPPs are lossy and leaky. Because the Γ point possesses C_{4v} symmetry [53], for the H matrix, the complex coupling constant is defined as α for the modes propagating in the same direction but β for the modes propagating in the perpendicular direction. They are complex provided both near- and far-field interactions are present [54]. In addition, for the in-coupling matrix K and the incident power S_+ , each mode supports only one input channel with an in-coupling constant defined as κ , and the incident power amplitudes are defined as s_{p+} and s_{s+} for p- and s-polarizations in

positive x and y directions. The sign of κ depends on the relative orientation between the incident polarization and the transverse polarization of the SPP, which lies in the plane defined by \vec{k}_{SPP} , resulting in 0 and π phase shift [54]. Four channels will interfere and yield a specular (total) reflection. Once Eq. (1) is formulated properly, we then solve the eigenvalues and eigenvectors by performing diagonalization. Eq. (1) can then be rewritten as [55]:

$$\frac{d}{dt} \begin{bmatrix} \tilde{a}_1 \\ \tilde{a}_2 \\ \tilde{a}_3 \\ \tilde{a}_4 \end{bmatrix} = i \begin{bmatrix} \tilde{\omega}_o - \alpha & 0 & 0 & 0 \\ 0 & \tilde{\omega}_o - \alpha & 0 & 0 \\ 0 & 0 & \tilde{\omega}_o + \alpha - 2\beta & 0 \\ 0 & 0 & 0 & \tilde{\omega}_o + \alpha + 2\beta \end{bmatrix} \begin{bmatrix} \tilde{a}_1 \\ \tilde{a}_2 \\ \tilde{a}_3 \\ \tilde{a}_4 \end{bmatrix} - \sqrt{2} \begin{bmatrix} 0 & \kappa \\ \kappa & 0 \\ 0 & 0 \\ 0 & 0 \end{bmatrix} \begin{bmatrix} s_{p+} \\ s_{s+} \end{bmatrix}, \quad (2)$$

where $[\tilde{a}_1 \quad \tilde{a}_2 \quad \tilde{a}_3 \quad \tilde{a}_4]^T = \begin{bmatrix} \frac{-a_3 + a_4}{\sqrt{2}} & \frac{-a_1 + a_2}{\sqrt{2}} & \frac{-a_1 - a_2 + a_3 + a_4}{2} & \frac{a_1 + a_2 + a_3 + a_4}{2} \end{bmatrix}^T$.

From Eq. (2), we see from the diagonalized H matrix that $\tilde{a}_{1,2}$ modes are degenerate with $\tilde{\omega}_{1,2} = \tilde{\omega}_o - \alpha$ but $\tilde{a}_{3,4}$ modes are nondegenerate with $\tilde{\omega}_{3,4} = \tilde{\omega}_o + \alpha \mp 2\beta$. Two energy band gaps thus are formed. Assuming a_{1-4} have the spatial form of $e^{i\vec{k}_{SPP} \cdot \vec{r}}$, or $e^{\pm i \frac{2\pi}{P} x}$ and $e^{\pm i \frac{2\pi}{P} y}$, their electric field magnitudes in the z direction, $E_z(x, y)$, can be roughly approximated as:

$$\begin{bmatrix} -\sqrt{2}i \sin(2\pi y/P) \\ -\sqrt{2}i \sin(2\pi x/P) \\ -\cos(2\pi x/P) + \cos(2\pi y/P) \\ \cos(2\pi x/P) + \cos(2\pi y/P) \end{bmatrix}, \text{ which are illustrated in Fig. 1(c). We see from the figure that}$$

the irreducible representations of $\tilde{a}_{1,2}$ are E whereas \tilde{a}_3 and \tilde{a}_4 are B_1 and A_1 following the C_{4v} character table [56]. In other words, $\tilde{a}_{1,2}$ (E) exhibit p_y and p_x characters and \tilde{a}_3 (B_1) and \tilde{a}_4 (A_1) display d_{xy} and s characters. From the diagonalized K matrix in Eq. (2), we also see the degenerate E modes are radiative bright modes that can be excited individually by s- and p-polarized lights. On the other hand, both A_1 and B_1 modes are symmetry protected bound states in the continuum (BICs) with zero in-coupling constants [29,57,58]. Although their angular frequencies are still complex due to the Ohmic absorption loss, the modes have zero radiative

decay rates and do not interact with far-field. To resolve A_1 and B_1 , we notice from Fig. 1(c) that they exhibit different field symmetries after rotating the patterns by 45° . It shows B_1 is asymmetric with respect to the Γ -M plane whereas A_1 is symmetric. Therefore, in the vicinity to the Γ point along the Γ -M direction where C_{4v} symmetry is broken and A_1 and B_1 are no longer BICs, B_1 is s-excited but A_1 is p-excited [59]. As a result, all the irreducible representations can be identified unambiguously at the Γ point, and we will verify them by FDTD and experiment.

At X point

At the X point taken under $\theta = \sin^{-1}(\lambda/2P)$ in the Γ -X direction, the four $(0, \pm 1)$ and $(-1, \pm 1)$ SPPs calculated by the phase matching equation are illustrated in Fig. 1(d) with $\vec{k}_{SPP} = \pm(\hat{x} \pm 2\hat{y})(\pi/P)$. We define the complex coupling constants to be η , γ , and σ for the modes oriented relatively to each other by 60° , 120° , and 180° , respectively. As the X point follows C_{2v} symmetry in which only two right- and left-hand diffractions are supported [53], the CMT equation can be expressed as:

$$\frac{d}{dt} \begin{bmatrix} a_1 \\ a_2 \\ a_3 \\ a_4 \end{bmatrix} = i \begin{bmatrix} \tilde{\omega}_o & \sigma & \gamma & \eta \\ \sigma & \tilde{\omega}_o & \eta & \gamma \\ \gamma & \eta & \tilde{\omega}_o & \sigma \\ \eta & \gamma & \sigma & \tilde{\omega}_o \end{bmatrix} \begin{bmatrix} a_1 \\ a_2 \\ a_3 \\ a_4 \end{bmatrix} + \begin{bmatrix} -\kappa_{pL} & \kappa_{sL} & -\kappa_{pR} & \kappa_{sR} \\ \kappa_{pR} & -\kappa_{sR} & \kappa_{pL} & -\kappa_{sL} \\ -\kappa_{pL} & -\kappa_{sL} & -\kappa_{pR} & -\kappa_{sR} \\ \kappa_{pR} & \kappa_{sR} & \kappa_{pL} & \kappa_{sL} \end{bmatrix} \begin{bmatrix} s_{pL+} \\ s_{sL+} \\ s_{pR+} \\ s_{sR+} \end{bmatrix}, \quad (3)$$

where the R and L subscripts in κ and s_+ represent the right and left incidences. After diagonalization, Eq. (3) is transformed as [55]:

$$\frac{d}{dt} \begin{bmatrix} \tilde{a}_1 \\ \tilde{a}_2 \\ \tilde{a}_3 \\ \tilde{a}_4 \end{bmatrix} = i \begin{bmatrix} \tilde{\omega}_o + \sigma - \gamma - \eta & 0 & 0 & 0 \\ 0 & \tilde{\omega}_o - \sigma + \gamma - \eta & 0 & 0 \\ 0 & 0 & \tilde{\omega}_o - \sigma - \gamma + \eta & 0 \\ 0 & 0 & 0 & \tilde{\omega}_o + \sigma + \gamma + \eta \end{bmatrix} \begin{bmatrix} \tilde{a}_1 \\ \tilde{a}_2 \\ \tilde{a}_3 \\ \tilde{a}_4 \end{bmatrix} + TK \begin{bmatrix} s_{pL+} \\ s_{sL+} \\ s_{pR+} \\ s_{sR+} \end{bmatrix}, \quad (4)$$

where the $T = \frac{1}{2} \begin{bmatrix} -1 & -1 & 1 & 1 \\ -1 & 1 & -1 & 1 \\ 1 & -1 & -1 & 1 \\ 1 & 1 & 1 & 1 \end{bmatrix}$ transformed in-coupling matrix TK is

$$\begin{bmatrix} 0 & \kappa_{sR} - \kappa_{sL} & 0 & -(\kappa_{sR} - \kappa_{sL}) \\ \kappa_{pR} + \kappa_{pL} & 0 & \kappa_{pR} + \kappa_{pL} & 0 \\ 0 & \kappa_{sR} + \kappa_{sL} & 0 & \kappa_{sR} + \kappa_{sL} \\ \kappa_{pR} - \kappa_{pL} & 0 & -(\kappa_{pR} - \kappa_{pL}) & 0 \end{bmatrix} \quad \text{and} \quad [\tilde{a}_1 \quad \tilde{a}_2 \quad \tilde{a}_3 \quad \tilde{a}_4]^T =$$

$$\frac{1}{2} [-a_1 - a_2 + a_3 + a_4 \quad -a_1 + a_2 - a_3 + a_4 \quad a_1 - a_2 - a_3 + a_4 \quad a_1 + a_2 + a_3 + a_4]^T. \quad \text{We see all the}$$

coupled modes are nondegenerate and three energy band gaps are formed. We also see all modes show different polarization dependences, with $\tilde{a}_{1,3}$ are s-excited but $\tilde{a}_{2,4}$ are p-excited.

The SPP field magnitudes of the coupled modes are calculated as $2 \begin{bmatrix} -\sin(\pi x/P) \sin(2\pi y/P) \\ i \sin(\pi x/P) \cos(2\pi y/P) \\ i \cos(\pi x/P) \sin(2\pi y/P) \\ \cos(\pi x/P) \cos(2\pi y/P) \end{bmatrix}$

in Fig. 1(e). Using the character table for C_{2v} point group, we assign \tilde{a}_1 and \tilde{a}_3 to be B_2 and A_2 and \tilde{a}_2 and \tilde{a}_4 to be B_1 and A_1 , respectively [56].

To resolve them accordingly, we formulate their right and left diffraction orders. By using conservation of energy and time reversal symmetry, the outgoing radiation channels are

expressed as $S_- = CS_+ + K^T T^T \tilde{A}$ or $\begin{bmatrix} S_{pL-} \\ S_{sL-} \\ S_{pR-} \\ S_{sR-} \end{bmatrix} = C \begin{bmatrix} S_{pL+} \\ S_{sL+} \\ S_{pR+} \\ S_{sR+} \end{bmatrix} + K^T T^T \begin{bmatrix} \tilde{a}_1 \\ \tilde{a}_2 \\ \tilde{a}_3 \\ \tilde{a}_4 \end{bmatrix}$, where C is the non-

resonant scattering matrix. Apparently, the radiations from \tilde{a}_{1-4} are manifested by $K^T T^T$, which results from the superposition between the radiations from the uncoupled a_{1-4} [55]. By taking only $s_{sR+} \neq 0$ under single right s-incidence, the diffraction orders are:

$$\begin{bmatrix} s_{pL-} \\ s_{sL-} \\ s_{pR-} \\ s_{sR-} \end{bmatrix} = C \begin{bmatrix} 0 \\ 0 \\ 0 \\ s_{sR+} \end{bmatrix} + \begin{bmatrix} 0 \\ -(\kappa_{sR} - \kappa_{sL})^2 \\ 0 \\ (\kappa_{sR} - \kappa_{sL})^2 \end{bmatrix} \frac{s_{sR+}}{i(\omega - \tilde{\omega}_1)} + \begin{bmatrix} 0 \\ (\kappa_{sR} + \kappa_{sL})^2 \\ 0 \\ (\kappa_{sR} + \kappa_{sL})^2 \end{bmatrix} \frac{s_{sR+}}{i(\omega - \tilde{\omega}_3)}, \quad (5)$$

showing only two diffractions at $\tilde{\omega}_1 = \tilde{\omega}_o + \sigma - \gamma - \eta$ (B₂) and $\tilde{\omega}_3 = \tilde{\omega}_o - \sigma - \gamma + \eta$ (A₂) are present and they both are s-polarized. In addition, while the left and right diffractions from B₂ are π out of phase, those from A₂ are in phase [29]. Likewise, for $s_{pR+} \neq 0$, we have

$$\begin{bmatrix} s_{pL-} \\ s_{sL-} \\ s_{pR-} \\ s_{sR-} \end{bmatrix} = C \begin{bmatrix} 0 \\ 0 \\ s_{pR+} \\ 0 \end{bmatrix} + \begin{bmatrix} (\kappa_{pR} + \kappa_{pL})^2 \\ 0 \\ (\kappa_{pR} + \kappa_{pL})^2 \\ 0 \end{bmatrix} \frac{s_{pR+}}{i(\omega - \tilde{\omega}_2)} + \begin{bmatrix} -(\kappa_{pR} - \kappa_{pL})^2 \\ 0 \\ (\kappa_{pR} - \kappa_{pL})^2 \\ 0 \end{bmatrix} \frac{s_{pR+}}{i(\omega - \tilde{\omega}_4)}, \quad (6)$$

indicating only p-polarized diffractions at $\tilde{\omega}_2 = \tilde{\omega}_o - \sigma + \gamma - \eta$ (B₁) and $\tilde{\omega}_4 = \tilde{\omega}_o + \sigma + \gamma + \eta$ (A₁) exist. The left and right diffractions are in phase for B₁ but π out of phase for A₁. Therefore, by measuring the diffractions under p- and s-incidences, we can identify A_{1,2} and B_{1,2}.

At M point

As illustrated in Fig. 1(f), four (0,0), (-1,0), (0,-1) and (-1,-1) SPPs couple at the M point with $\vec{k}_{spp} = \pm(\hat{x} \pm \hat{y})\pi/P$, which is the same as that of the Γ point after 45° rotation [53]. As a result, the functional forms of the diagonalized H and A remain the same in which $\tilde{a}_{1,2}$ modes

are degenerate but $\tilde{a}_{3,4}$ modes are not. The field patterns of \tilde{a}_{1-4} are
$$\begin{bmatrix} i\sqrt{2}\sin((x-y)\pi/P) \\ -i\sqrt{2}\sin((x+y)\pi/P) \\ -2\sin(\pi x/P)\sin(\pi y/P) \\ 2\cos(\pi x/P)\cos(\pi y/P) \end{bmatrix}$$

in Fig. 1(g). However, as the modes lie below the light cone, they do not interact with the continuum and can only be excited by near-field. Nevertheless, following the C_{4v} character table, $\tilde{a}_{1,2}$ are E whereas \tilde{a}_3 and \tilde{a}_4 are B₂ and A₁ [56].

III. FINITE-DIFFERENCE TIME DOMAIN SIMULATION

We perform FDTD simulations to verify the CMT results at the Γ and X points above the light cone as well as the M point below it. A series of 2D semi-infinitely thick Au square lattice nanohole arrays with $P = 750$ nm, hole height $H = 100$ nm, and hole radius R spanning from 150 to 300 nm are excited by polarized plane wave and dipole excitations to simulate their diffraction spectra and electric near-field patterns at and near the HSPs.

At Γ point

Fig. 2(a) & (c) show the p-polarized total reflectivity spectral mappings taken along the Γ -X direction, i.e. $\varphi = 0^\circ$, at $\theta = 0^\circ$ (Γ point) and 1° for different R . One sees at the Γ point, only one reflection dip is observed, and its spectral position varies slowly with R . Several spectra for $R = 150, 200, 250$, and 300 nm are extracted in Fig. S4-7 in the Supplementary Information, indicating the reflectivity dip depth decreases with increasing R [55]. On the other hand, for $\theta = 1^\circ$ where C_{4v} symmetry is broken, two more dips are seen, suggesting they are BICs at the Γ point. By comparing two mappings, one can conclude while the mode at $\theta = 0^\circ$ can be assigned as E, two additional modes at $\theta = 1^\circ$ are A_1 and B_1 . More importantly, we notice A_1 and B_1 locate at energies higher than E but gradually shift down as R increases. Therefore, E crosses with A_1 and B_1 at $R = 220$ and 270 nm, leading to two band inversions that may change the band topology. Fig. 2(b) & (d) show the corresponding s-polarized reflectivity mappings for $\theta = 0^\circ$ and 1° , in which only one reflection dip is observed despite broken symmetry. Several spectra are plotted in Fig. S4-7 for reference [55]. Clearly, the mode is found to be degenerate with E and thus is identified as the second E mode. We then calculate the field patterns of the E modes in Fig. S4-7, and they are consistent with Fig. 1(c) that the modes are p-like [55].

Once the radiative E modes are resolved, we then proceed to assign A_1 and B_1 . Fig. 2(e) & (f) show the p- and s-polarized reflectivity mappings taken at $\theta = 1^\circ$ along the Γ -M direction.

In agreement with CMT, two modes are excited by p- and s-polarized lights independently. The p-excited mode is assigned as A_1 whereas the s-excited one is B_1 . Their field patterns in Fig. S4-7 agree with those in Fig. 1(c) [55]. Therefore, by carrying out polarization-dependent reflectivity spectroscopy along the Γ -X and Γ -M directions, one can identify A_1 , B_1 , and E unambiguously in Fig. 2. Apparently, the crossings of B_1 and A_1 with E at $R = 220$ and 270 nm, respectively, result in the first and second band inversions. In contrast to the well-known 2D SSH model where band inversion is absent at the Γ point, our results demonstrate genuine photonic systems that go beyond the tight-binding framework [30,31]. The band inversions are expected to manifest very subtle changes in the band topology.

At X point

We show the p- and s-polarized total reflectivity spectral mappings taken at the X point along the Γ -X direction for different R in Fig. 3(a) & (b). Two figures indicate four nondegenerate modes are supported with a pair of modes is excited under one polarization. The spectra for $R = 150, 200, 250$ and 300 nm are extracted in Fig. 4(a)-(d) to further confirm the nondegeneracy. Therefore, one can assign A_1 and B_1 and A_2 and B_2 for the modes in p- and s-excited mappings. We notice from the Fig. 3(a) & (b) that A_1 and B_1 and A_2 and B_2 undergo one band inversion when R increases. However, all modes together lead to multiple band inversions. Such band inversions are different from those reported by Liu and Wakabayashi for 2D SSH model in which the lowest nonradiative X point is studied [30,31]. The corresponding field patterns of all four modes are calculated in Fig. S9-12 and they agree well with CMT in Fig. 1(e) [55].

We then resolve A_1 and B_1 and A_2 and B_2 by first simulating the p- and s-polarized specular reflectivity (r_0) and -1st diffraction order (r_{-1}) spectra for $R = 150, 200, 250$, and 300 nm in Fig. 4(e)-(l). For p-polarization, we then rewrite Eq. (6) for $r_{p,0}$ and $r_{p,-1}$ coefficients as two superimposed Lorentzian profiles given as [29,55]:

$$\begin{bmatrix} r_{p,0} \\ r_{p,-1} \end{bmatrix} = \begin{bmatrix} p_{0,b} \\ ip_{-1,b} \end{bmatrix} + \begin{bmatrix} \frac{\delta}{i(\omega - \tilde{\omega}_+)} - \frac{\gamma}{i(\omega - \tilde{\omega}_-)} \\ d \left(\frac{\delta}{i(\omega - \tilde{\omega}_+)} + \frac{\gamma}{i(\omega - \tilde{\omega}_-)} \right) \end{bmatrix} \quad (7)$$

where $p_{0,b}$ and $p_{-1,b}$ are the nonresonant backgrounds, $\tilde{\omega}_-$ and $\tilde{\omega}_+$ are the complex angular frequencies of the coupled modes, and δ and τ are the constants. The symmetry factor d is either 1 or -1, which determines whether $\tilde{\omega}_+$ mode is A_1 or B_1 . For example, if d is found to be 1, two diffraction orders from $\tilde{\omega}_+$ are in phase and thus $\tilde{\omega}_+$ is B_1 ($\tilde{\omega}_2$) whereas $\tilde{\omega}_-$ is A_1 ($\tilde{\omega}_4$). On the other hand, if $d = -1$, then two diffraction orders from $\tilde{\omega}_+$ are π out of phase, and $\tilde{\omega}_+$ and $\tilde{\omega}_-$ are A_1 ($\tilde{\omega}_4$) and B_1 ($\tilde{\omega}_2$), respectively. Likewise, for s-polarized $r_{s,0}$ and $r_{s,-1}$ coefficients, Eq. (5) is rewritten as [55]:

$$\begin{bmatrix} r_{s,0} \\ r_{s,-1} \end{bmatrix} = \begin{bmatrix} s_{0,b} \\ is_{-1,b} \end{bmatrix} + \begin{bmatrix} \frac{\mu}{i(\omega - \tilde{\omega}_+)} + \frac{\varepsilon}{i(\omega - \tilde{\omega}_-)} \\ d \left(\frac{\mu}{i(\omega - \tilde{\omega}_+)} - \frac{\varepsilon}{i(\omega - \tilde{\omega}_-)} \right) \end{bmatrix} \quad (8)$$

where $s_{0,b}$ and $s_{-1,b}$ are the nonresonant backgrounds and μ and ε are the constants. $\tilde{\omega}_+$ is A_2 ($\tilde{\omega}_3$) when $d = 1$ but is B_2 ($\tilde{\omega}_1$) for $d = -1$.

We then fit the spectra in Fig. 4(e)-(l) by using $|r_{p/s,0}|^2$ and $|r_{p/s,-1}|^2$ from Eq. (7) & (8) and the best fits are shown as dash lines. While $p/s_{0,b}$ and $p/s_{-1,b}$ are determined from the non-resonant regions, their phase difference is known to be $-\pi/2$ [60,61]. The best fitted parameters are tabulated in Table 1, showing d gradually flips from -1(-1) for p-(s-) polarization but to 1(1) when R increases. It indicates, for p-polarization, A_1 and B_1 are located at higher and lower energies at small R but switch places as R increases. They undergo a band inversion at around $R \sim 250$ nm. Such flip is consistent with the switch of the FDTD field patterns in Fig. S9-12 [55]. Likewise, for s-polarization, B_2 and A_2 are located at higher and lower energies at

small R but go through a band inversion also at $R \sim 230$ nm. As a result, the irreducible representations, $A_{1,2}$ and $B_{1,2}$, are labelled in Fig. 3(a) & (b) and they agree with CMT.

At M point

As the modes at the M point are below the light cone, they cannot be accessed by far-field. Therefore, dipole excitation is used for calculating the p- and s-polarized radiation spectral mappings as a function of R in Fig. 5(a) & (b). All four nonradiative modes are seen, and they resemble to the results of the Γ point. Two degenerate modes are assigned as E whereas other two nondegenerate are identified as A_1 and B_2 following the field patterns illustrated in Fig. S14-16 [55]. We notice that E and B_2 are about to merge at $R = 300$ nm, possibly yielding a Dirac point and band inversion at larger R .

IV. EXPERIMENTAL VERIFICATION

We verify our theory by conducting angle- and polarization-resolved diffraction spectroscopy on three 2D Au nanohole PmCs fabricated by focused ion beam (FIB). Their plane-view scanning electron microscopy (SEM) images are shown in the insets of Fig. 6(b), (d) & (f), showing they have $P = 753$ nm, $H = 102$ nm, and $R = 150, 250$, and 300 nm. We chose these hole radii because they are located before and after two band inversions in Fig. 2. After sample preparation, the PmCs are then transferred to a homebuilt Fourier space optical microscope described in the Supplementary Information for measurements [29,48,55]. Briefly, a supercontinuum generation laser is illuminated on the sample at a well-defined incident angle θ via the microscope objective lens and the signals reflected from the sample are collected by the same objective lens in which the diffraction orders are projected onto the momentum space. By using an aperture to filter out the desired diffraction order, a spectrometer-based CCD detector is used for measuring the diffraction spectra. The PmCs are placed on a rotatable sample stage for azimuthally changing ϕ .

At Γ point

The p- and s-polarized angle-resolved specular (total) reflectivity mappings of three PmCs taken along the Γ -X direction are illustrated in Fig. 6. The SPP dispersions are sketched as dash lines in Fig. 6(a) & (b) for visualization. We see the dispersion relations behave the same for all PmCs at $\theta > \pm 1^\circ$. While the $(\pm 1, 0)$ SPPs are p-excited, two degenerate $(0, \pm 1)$ modes are p- and s-excited. The degenerate modes are labelled as symmetric $(0, \pm 1)_s$ and asymmetric $(0, \pm 1)_a$ SPPs, respectively, due to their distinctive field symmetries in the y-direction [59].

However, when approaching to the Γ point, the mode dispersions are found to be strongly R dependent. We expect the band assignments are different for different PmCs. For the $R = 150$ nm PmC in Fig. 6(a) & (b), as indicated by the red dash line, we see the p-excited $(-1, 0)$ and s-excited $(0, \pm 1)_a$ SPPs located at 784 nm are degenerate, and they are assigned as E. On the other hand, the $(1, 0)$ and $(0, \pm 1)_s$ SPPs vanish at the Γ point, forming two BICs at 761 and 778 nm. It is noticed that the band gap between the $(-1, 0)$ and $(0, \pm 1)_s$ SPPs is very small, making the $(0, \pm 1)_s$ BIC difficult to be resolved. To assign the $(1, 0)$ and $(0, \pm 1)_s$ SPPs properly, the corresponding p- and s-polarized angle-resolved reflectivity mappings taken along the Γ -M direction are shown in Fig. 7(a) & (b). The SPP dispersions are sketched as dash lines. One can see that the $(1, 0)$ and $(0, \pm 1)_s$ SPPs are BICs at 0° but become visible when θ increases. Essentially, the $(1, 0)$ and $(0, \pm 1)_s$ SPPs are p- and s-excited, and thus are assigned as A_1 and B_1 . Therefore, the irreducible representations from high to low energy are A_1 , B_1 , and E, which agree with FDTD simulation.

For the $R = 250$ nm PmC, its p- and s-mappings are shown in Fig. 6(c) & (d), clearly indicating two band gaps are present and two BICs, arising from the $(\pm 1, 0)$ SPPs, are observed at 760 and 797 nm. In addition, the $(0, \pm 1)_s$ and $(0, \pm 1)_a$ SPPs at 774 nm are degenerate, revealing they are the E modes. To assign the $(\pm 1, 0)$ SPPs, we examine the p- and s-mappings

in the Γ -M direction in Fig. 7(c) & (d). The $(\pm 1, 0)$ SPPs are no longer BICs as θ increases. As the $(1, 0)$ and $(-1, 0)$ SPPs are p- and s-excited, they are assigned as A_1 and B_1 . The descending order thus is A_1 , E, and B_1 , showing one band inversion occurs between E and B_1 .

For the $R = 300$ nm PmC in Fig. 6(e) & (f), we notice the p-excited $(1, 0)$ and s-excited $(0, \pm 1)_a$ SPPs are degenerate at 767 nm, and are the E modes. The $(-1, 0)$ and $(0, \pm 1)_s$ SPPs are two BICs located at 774 and 791 nm. Fig. 7(e) & (f) show while the $(-1, 0)$ mode is s-excited, the $(0, \pm 1)_s$ mode is p-excited, making them as B_1 and A_1 . As a result, the irreducible representations are E, A_1 , and B_1 in which E and A_1 undergo the second band inversion. All results at the Γ point agree with the FDTD results.

At X point

We examine the p- and s-polarized angle-resolved specular reflectivity mappings of the PmCs taken around the X point in the Γ -X direction in Fig. 8(a)-(f). The dispersion relations are sketched in Fig. 8(a) & (b), showing two p-excited $(0, \pm 1)_s$ and $(-1, \pm 1)_s$ SPPs that are A_1 and B_1 and s-excited $(0, \pm 1)_a$ and $(-1, \pm 1)_a$ that are A_2 and B_2 . All of them are nondegenerate. We see the crossing of $(0, \pm 1)_s$ and $(-1, \pm 1)_s$ as well as $(0, \pm 1)_a$ and $(-1, \pm 1)_a$ yield a band gap at $\sim \theta = 25^\circ$. Again, similar to those at the Γ point, the dispersions of three PmCs near the X point behave differently for different R, showing the band assignments are strongly R dependent.

For the $R = 150$ nm PmC, from Fig. 8(a) & (b) at the X point, they show the p-polarized higher and lower energy SPPs locate at 682 and 700 nm whereas the s-excited higher and lower energy SPPs position at 698 and 715 nm. We then plot the corresponding p- and s-polarized specular reflectivity and -1st diffraction order spectra in Fig. 9(a) & (b) and fit them by using Eq. (7) & (8) with the best fits displayed as dash lines. The fitted parameters are tabulated in Table 2, revealing $d = -1$ for p-polarization but -1 and for s-polarization. Therefore, two diffraction orders from the p-excited higher and lower energy modes are π out of phase and in phase, and they are assigned as A_1 and B_1 . On the other hand, two diffraction orders from the

s-excited higher and lower modes are π out of phase and in phase, and the modes are assigned as B_2 and A_2 . The irreducible representations are A_1 , B_2 , B_1 , and A_2 .

On the other hand, for the $R = 250$ nm PmC, the p-excited higher and lower energy modes are located at 690 and 707 nm and the s-excited higher and lower energy modes are positioned at 687 and 710 nm at the X point in Fig. 8(c) & (d). Their corresponding p- and s-polarized diffraction spectra and the best fits are shown in Fig. 9(c) & (d). Table 2 shows $d = 1$ and 1 for p- and s-polarizations. As a result, the p-polarized higher and lower energy modes are B_1 and A_1 whereas the s-excited higher and lower energy modes are A_2 and B_2 . Compared with the $R = 150$ PmC, the irreducible representations are A_2 , B_1 , A_1 , and B_2 in which both A_1 and B_1 as well as A_2 and B_2 undergo band inversions.

Finally, for the $R = 300$ nm PmC, the p- and s-excited higher and lower energy modes are found at 696 and 715 nm as well as 677 and 706 nm at the X point from Fig. 8(e) & (f). The corresponding p- and s-polarized specular reflectivity and -1st diffraction order spectra are shown in Fig. 9(e) & (f) and the best fits are displayed as dash lines. Table 2 shows $d = 1$ and 1 for p- and s-polarizations and the p-excited higher and lower energy modes are B_1 and A_1 and the s-excited higher and lower energy modes are A_2 and B_2 . The descending order of the irreducible representations is A_2 , B_1 , B_2 , and A_1 . Band flipping occurs between A_1 and B_2 .

V. CONCLUSION

In summary, we have determined the irreducible representations of the energy bands at the HSPs in the Brillouin zone of 2D square lattice photonic systems. By using temporal coupled mode theory (CMT) to study how the photonic modes interact with each other and with the continuum at the HSPs, we formulate a far-field approach that enables us to resolve the field symmetries of the photonic modes accordingly. Both our numerical and experimental results based on angle- and polarization-resolved diffraction spectroscopy agree very well with CMT. Our results demonstrate, for 2D nanohole plasmonic arrays for different hole radii, the

modes at the Γ and X points undergo subtle band inversions when the radius increases, revealing a complicated dependence of band topology on system geometry. The band inversions go beyond the well-known 2D SSH model, posing new ways in probing the topological properties of non-Hermitian electromagnetic systems and designing and realizing their topologically protected edge and corner states.

VI. ACKNOWLEDGEMENT

This research was supported by the Chinese University of Hong Kong through Innovative Technology Fund Guangdong-Hong Kong Technology Cooperation Funding Scheme (GHP/077/20GD), Partnership Research Program (PRP/048/22FX), and Seed Program (ITS/245/23).

Reference

1. X.L. Qi and S.C. Zhang, Topological insulators and superconductors, *Rev. Mod. Phys.* 83, 1057 (2011).
2. T. Shah, C. Brendel, V. Peano, and F. Marquardt, Topologically protected transport in engineered mechanical systems, *Rev. Mod. Phys.* 96, 021002 (2024).
3. S.D. Huber, Topological mechanics, *Nat. Phys.* 12, 621 (2016).
4. B. Xie, H.F. Wang, X.Y. Zhu, M.H. Lu, Z.D. Wang, and Y.F. Chen, Photonics meets topology, *Opt. Exp.* 26, 24531 (2018).
5. A.B. Khanikaev and A. Alù, Topological photonics: robustness and beyond, *Nat. Comm.* 15, 931 (2024).
6. C.H. Lee, S. Imhof, C. Berger, F. Bayer, J. Brehm, L.W. Molenkamp, T. Kiessling, and R. Thomale, Topoelectrical circuits *Comm. Phys.* 1, 39 (2018).
7. H. Yang, L. Song, Y. Cao, and P. Yan, Circuit realization of topological physics, *Phys. Rep.* 1093, 1 (2024).
8. M.Z. Hasan and C.L. Kane, Topological insulators, *Rev. Mod. Phys.* 82, 3045 (2010).
9. J.E. Moore, The birth of topological insulators, *Nature* 464, 194 (2010).
10. O. Breunig and Y. Ando, Opportunities in topological insulator devices, *Nat. Rev. Phys.* 4, 184 (2022).
11. G. Ma, M. Xiao and C.T. Chan, Topological phases in acoustic and mechanical systems, *Nat. Rev. Phys.* 1, 281 (2019).
12. X. Zhang, M. Xiao, Y. Cheng, M. Lu, and J. Christensen, Topological sound, *Comm. Phys.* 1, 97 (2018).
13. H. Xue, Y. Yang, and B. Zhang, Topological acoustics, *Nat. Rev. Mater.* 7, 974 (2022).
14. T. Ozawa, H.M. Price, A. Amo, N. Goldman, M. Hafezi, L. Lu, M.C. Rechtsman, D. Schuster, J. Simon, O. Zilberberg, and I. Carusotto, Topological photonics, *Rev. Mod. Phys.* 91, 015006 (2019).
15. L. Lu, J.D. Joannopoulos and M. Soljačić, Topological photonics, *Nat. Photon.* 8, 821 (2018).
16. A.B. Khanikaev and G. Shvets, Two-dimensional topological photonics, *Nat. Photon.* 11, 763 (2017).
17. G. Tang, X. He, F. Shi, J. Liu, X. Chen, and J. Dong, Topological Photonic Crystals: Physics, Designs, and Applications, *Laser & Photon. Rev.* 16, 2100300 (2022).
18. L. Wu and X. Hu, Scheme for Achieving a Topological Photonic Crystal by Using Dielectric Material, *Phys. Rev. Lett.* 114, 223901 (2015)
19. Z. Lan, M.N. Chen, F. Gao, S. Zhang, and W.E.I. Sha, A brief review of topological photonics in one, two, and three dimensions, *Rev. Phys.* 9, 100076 (2022).
20. X. Ni, S. Yves, A. Krasnok, and A. Alù, Topological metamaterials, *Chem. Rev.* 123, 12, 7585 (2023).
21. C. Liu and H.C. Ong, Realization of topological superlattices and the associated interface states in one-dimensional plasmonic crystals, *Phys. Rev. B* 106, 045401 (2022).
22. M.S. Rider, Á. Buendía, D.R. Abujetas, P.A. Huidobro, J.A. Sánchez-Gil, and V. Giannini, Advances and Prospects in Topological Nanoparticle Photonics, *ACS Photon.* 9, 1483 (2022).
23. M. Atala, M. Aidelsburger, J.T. Barreiro, D. Abanin, T. Kitagawa, E. Demler and I. Bloch, Direct measurement of the Zak phase in topological Bloch bands, *Nat. Phys.* 9, 795 (2013).
24. W. P. Su, J. R. Schrieffer, and A. J. Heeger, Solitons in Polyacetylene, *Phys. Rev. Lett.* 42, 1698 (1979).
25. J. Zak, Berry's Phase for Energy Bands in Solids, *Phys. Rev. Lett.* 62, 2747 (1989).

26. M. Xiao, Z.Q. Zhang, and C.T. Chan, Surface impedance and bulk band geometric phases in one-dimensional systems, *Phys. Rev. X* 4, 021017 (2014).
27. M. Xiao, G. Ma, Z. Yang, P. Sheng, Z.Q. Zhang, and C.T. Chan, Geometric phase and band inversion in periodic acoustic systems, *Nat. Phys.* 11, 240 (2015).
28. J.K. Asbóth, L. Oroszlány, and A. Pályi, *A Short Course on Topological Insulators* (Springer, New York, 2016).
29. C. Liu, H. R. Wang, and H. C. Ong, Determination of the Zak phase of one-dimensional diffractive systems with inversion symmetry via radiation in Fourier space, *Phys. Rev. B* 108, 035403 (2023).
30. F. Liu and K. Wakabayashi, Novel topological phase with a zero Berry curvature, *Phys. Rev. Lett.* 118, 076803 (2017).
31. F. Liu, H. Deng, and K. Wakabayashi, Topological photonic crystals with zero Berry curvature, *Phys. Rev. B* 97, 035442 (2018).
32. X. Chen, W. Deng, F. Shi, F. Zhao, M. Chen, and J. Dong, Direct observation of corner states in second-order topological photonic crystal slabs, *Phys. Rev. Lett.* 122, 233902 (2019).
33. B. Xie, G. Su, H. Wang, H. Su, X.P. Shen, P. Zhan, M. Lu, Z. Wang, and Y.F. Chen, Visualization of higher-order topological insulating phases in two-dimensional dielectric photonic crystals, *Phys. Rev. Lett.* 122, 233903 (2019).
34. H. Ma, Z. Zhang, P. Fu, J. Wu, and X.-L. Yu, Electronic and topological properties of extended two-dimensional Su-Schrieffer-Heeger models and realization of flat edge bands, *Phys. Rev. B* 106, 245109 (2022).
35. M. Kim and J. Rho, Topological edge and corner states in a two-dimensional photonic Su-Schrieffer-Heeger lattice, *Nanophotonics*, 9, 3227 (2020).
36. X. Luo, X. Pan, C. Liu, and X. Liu, Higher-order topological phases emerging from Su-Schrieffer-Heeger stacking, *Phys. Rev. B* 107, 045118 (2023).
37. L. Zheng, V. Achilleos, O. Richoux, G. Theocharis, and V. Pagneux, Observation of edge waves in a two-dimensional Su-Schrieffer-Heeger acoustic network, *Phys. Rev. Applied* 12, 034014 (2019).
38. M. Jin, Y. Gao, H. Lin, Y. He, and M. Chen, Corner states in second-order two-dimensional topological photonic crystals with reversed materials, *Phys. Rev. A* 106, 013510 (2022).
39. B. Bradlyn, L. Elcoro, J. Cano, M.G. Vergniory, Z. Wang, C. Felser, M.I. Aroyo, and B.A. Bernevig, Topological quantum chemistry, *Nature* 547, 298 (2017).
40. M. Blanco de Paz, M.G. Vergniory, D. Bercioux, A. García-Etxarri, and B. Bradlyn, Engineering fragile topology in photonic crystals: Topological quantum chemistry of light, *Phys. Rev. Research* 1, 032005(R) (2019).
41. S. Vaidya, A. Ghorashi, T. Christensen, M.C. Rechtsman, and W.A. Benalcazar, Topological phases of photonic crystals under crystalline symmetries, *Phys. Rev. B* 108, 085116 (2023).
42. J. Cano, B. Bradlyn, Z. Wang, L. Elcoro, M.G. Vergniory, C. Felser, M.I. Aroyo, and B.A. Bernevig, Topology of disconnected elementary band representations, *Phys. Rev. Lett.* 120, 266401 (2018).
43. J. Cano, B. Bradlyn, Z. Wang, L. Elcoro, M.G. Vergniory, C. Felser, M.I. Aroyo, and B.A. Bernevig, Building blocks of topological quantum chemistry: Elementary band representations, *Phys. Rev. B* 97, 035139 (2018).
44. M.A. Gorlach, X. Ni, D.A. Smirnova, D. Korobkin, D. Zhirihin, A.P. Slobozhanyuk, P.A. Belov, A. Alù, and A.B. Khanikaev, Far-field probing of leaky topological states in all dielectric metasurfaces, *Nat. Comm.* 9, 909 (2018).
45. W. Gao, M. Xiao, C.T. Chan, and W.Y. Tam, Determination of Zak phase by reflection phase in 1D photonic crystals, *Opt. Lett.* 40, 5259 (2015).

46. Q. Wang, M. Xiao, H. Liu, S. Zhu, and C.T. Chan, Measurement of the Zak phase of photonic bands through the interface states of a metasurface/photonic crystal, *Phys. Rev. B* 93, 041415(R) (2016).
47. F. Bleckmann, Z. Cherpakova, S. Linden, and A. Alberti, Spectral imaging of topological edge states in plasmonic waveguide arrays, *Phys. Rev. B* 96, 045417 (2017).
48. X. Guo, C. Liu, and H. C. Ong, Generalization of the circular dichroism from metallic arrays that support Bloch-like surface plasmon polaritons, *Phys. Rev. Appl.* 15, 024048 (2021).
49. C. Ropers, D. J. Park, G. Stibenz, G. Steinmeyer, J. Kim, D. S. Kim, and C. Lienau, Femtosecond light transmission and subradiant damping in plasmonic crystals, *Phys. Rev. Lett.* 94 113901 (2005).
50. H. A. Haus, *Waves and fields in optoelectronics* (Prentice-Hall, New Jersey, 1984).
51. S. Fan, in *Optical Fiber Telecommunications V*, edited by I. P. Kaminow, T. Li, and A. E. Willner (Academic Press, Burlington, 2008).
52. L. Verslegers, Z. Yu, Z. Ruan, P. B. Catrysse, and S. H. Fan, From electromagnetically induced transparency to superscattering with a single structure: A coupled-mode theory for doubly resonant structures, *Phys. Rev. Lett.* 108, 083902 (2012).
53. Y. Zhang, A. Chen, W.H. Liu, C.W. Hsu, B. Wang, F. Guan, X. Liu, L. Shi, L. Lu, and J. Zi, Observation of polarization vortices in momentum space, *Phys. Rev. Lett.* 120, 186103 (2018).
54. Z.L. Cao, L.Y. Yiu, Z.Q. Zhang, C.T. Chan, and H. C. Ong, Understanding the role of surface plasmon polaritons in two-dimensional achiral nanohole arrays for polarization conversion, *Phys. Rev. B* 95, 155415 (2017).
55. See Supplementary Information for the CMT formulations at the Γ and X points, the FDTD simulation results at the Γ , X and M points, and the descriptions of the measurement setup.
56. K. Sakoda, *Optical Properties of Photonic Crystals* (Springer, New York, 2005).
57. K. Koshelev, A. Bogdanov, and Y. Kivshar, Engineering with bound states in the continuum, *Opt. Photon. News* 31, 38 (2020).
58. C.W. Hsu, B. Zhen, A.D. Stone, J.D. Joannopoulos, and M. Soljacic, Bound states in the continuum, *Nat. Rev. Mater.* 1, 16048 (2016).
59. J.T.K. Wan, H. Iu, and H.C. Ong, Structural symmetry of two-dimensional metallic arrays: Implications for surface plasmon excitations, *Opt. Comm.* 283, 1546 (2010).
60. C.M. B. Cordeiro, L. Cescato, A.A. Freschi, and L. Li, Measurement of phase differences between the diffracted orders of deep relief gratings, *Opt. Lett.* 28, 683 (2003).
61. N. Destouches, H. Giovannini, and M. Lequime, Interferometric measurement of the phase of diffracted waves near the plasmon resonances of metallic gratings, *Appl. Opt.* 40, 5575 (2001).

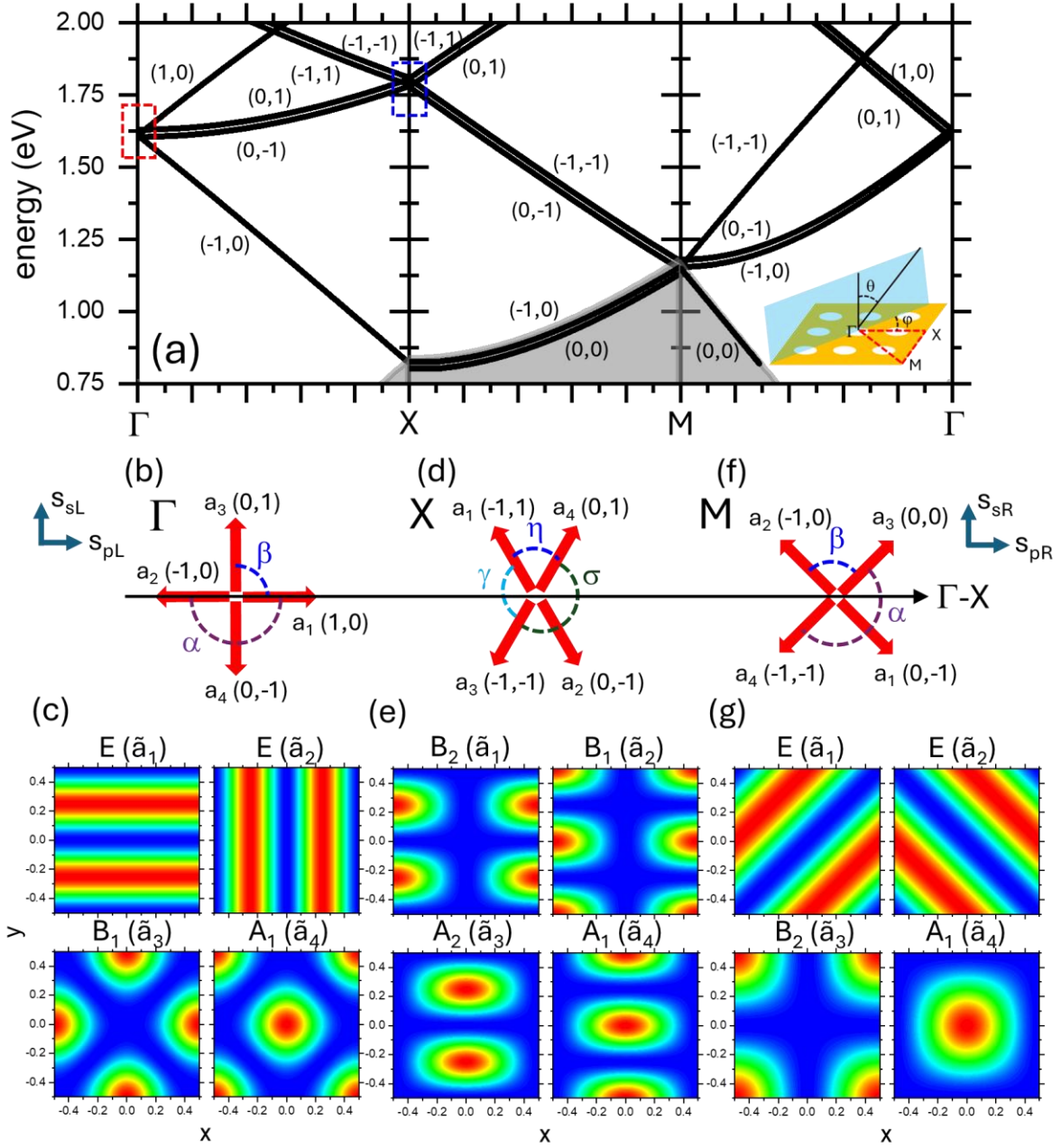


Fig. 1. (a) The dispersion relations of 2D square lattice PmC in the Brillouin zone. The double degeneracy is offset slightly for visualization. Energy band gaps are expected to form at the Γ , X, and M points where the Bloch-like SPPs couple. The grey area is the light cone. Inset: the square lattice and the excitation condition. (b) At the Γ point, the schematic of how four $(\pm 1, 0)$ and $(0, \pm 1)$ SPPs couple for CMT formulation and the coupling constants are defined as α and β . (c) The CMT deduced field patterns of \tilde{a}_{1-4} and are labelled as E, B_1 , and A_1 . (d) At the X point, the schematic of how four $(0, \pm 1)$ and $(-1, \pm 1)$ SPPs couple for CMT formulation and the coupling constants are defined as η , γ , and σ . (e) The field patterns of \tilde{a}_{1-4} and are labelled as B_2 , B_1 , A_2 , and A_1 . (f) At the M point, the schematic of how four $(0, 0)$, $(-1, 0)$, $(0, -1)$ and $(-1, -1)$ SPPs couple for CMT formulation and the coupling constants are defined as α and β . (g) The field patterns of \tilde{a}_{1-4} and are labelled as E, B_2 , and A_1 .

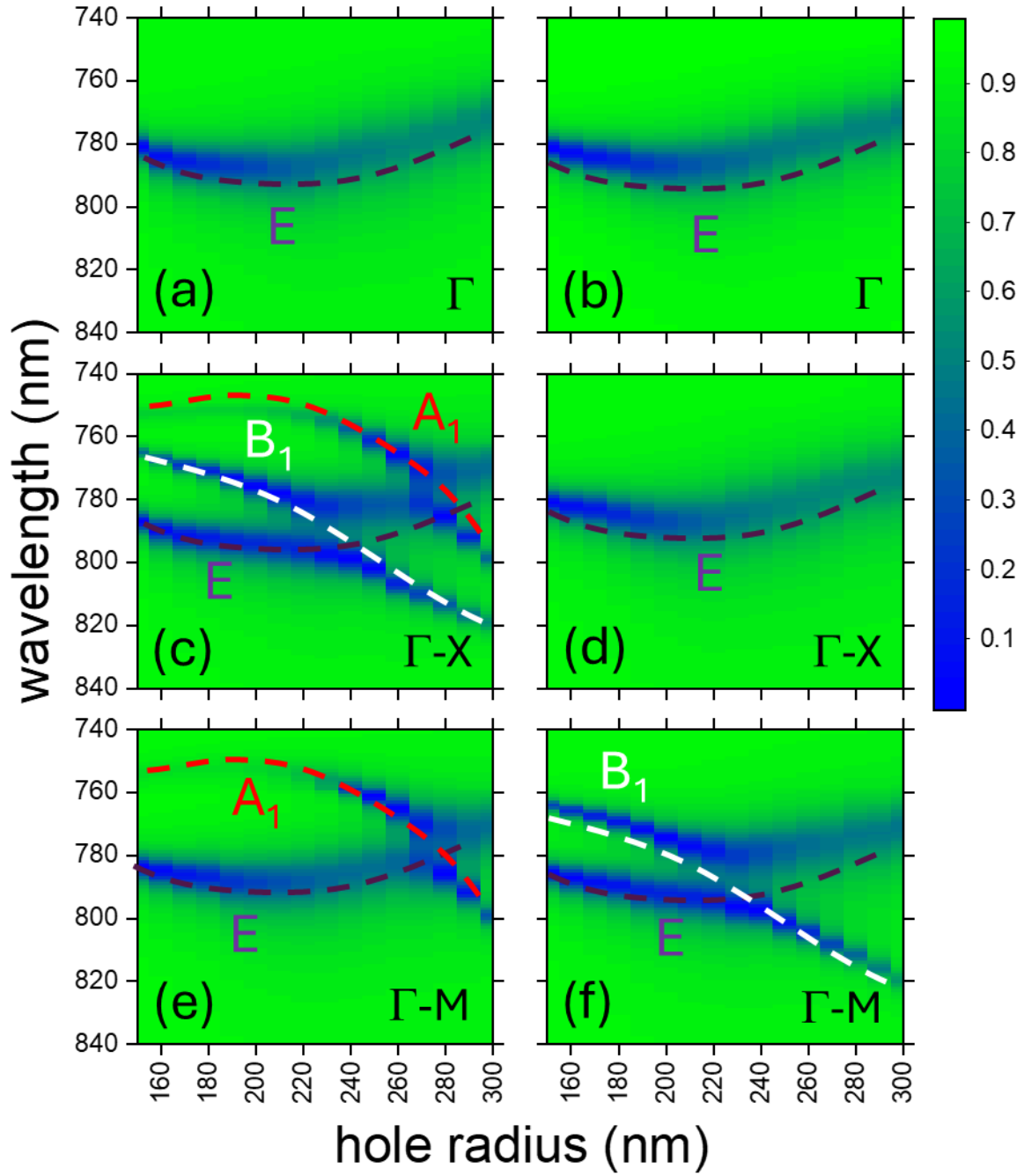


Fig. 2. The plots of the FDTD simulated (a) p- and (b) s-polarized specular (total) reflectivity mappings taken at the Γ point, where $\theta = 0^\circ$, as a function of R . The plots of the FDTD simulated (c) p- and (d) s-polarized reflectivity mappings taken along the Γ -X direction at $\theta = 1^\circ$ as a function of R . The plots of the FDTD simulated (e) p- and (f) s-polarized reflectivity mappings taken along the Γ -M direction at $\theta = 1^\circ$ as a function of R . The color dash lines are for the visualization of the A_1 , B_1 , and E assignments.

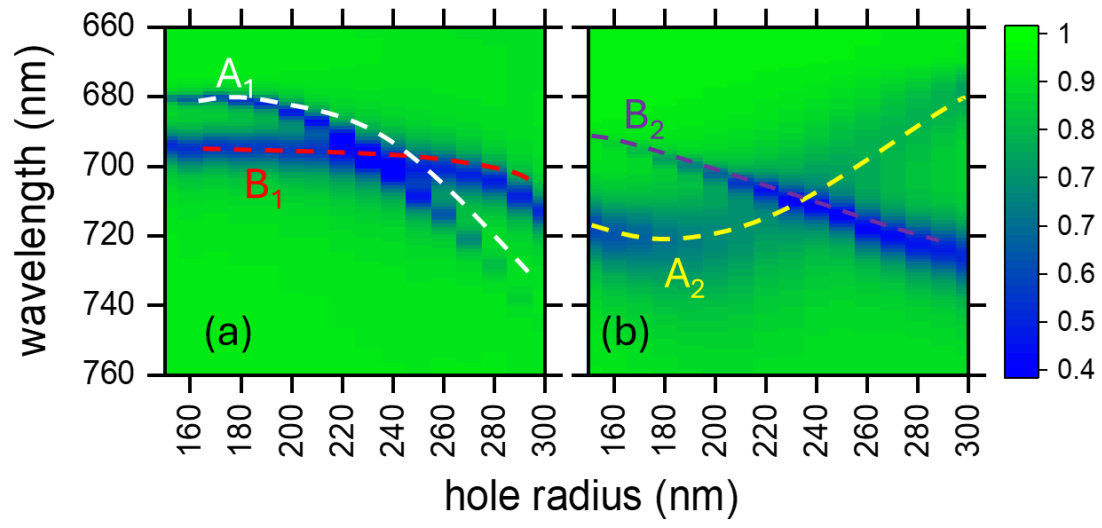


Fig. 3. The plots of the FDTD simulated (a) p- and (b) s-polarized total reflectivity mappings taken at the X point as a function of R . The color dash lines are for the visualization of the A_1 , B_1 , A_2 and B_2 assignments.

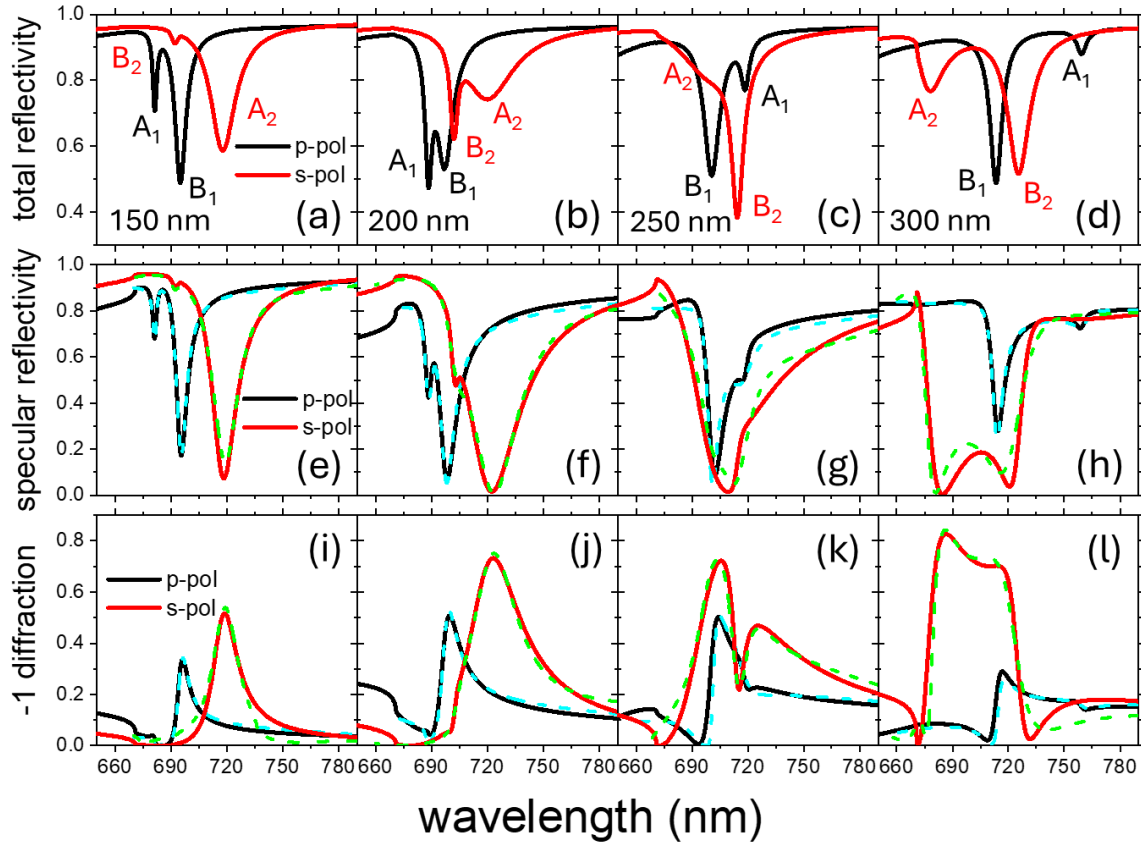


Fig. 4. The (black) p- and (red) s-polarized total reflectivity spectra taken at the X point for $R =$ (a) 150, (b) 200, (c) 250, and (d) 300 nm. The (black) p- and (red) s-polarized specular reflectivity spectra taken at the X point for $R =$ (e) 150, (f) 200, (g) 250, and (h) 300 nm. The best fits are displayed as dash lines. The (black) p- and (red) s-polarized -1st diffraction order spectra taken at the X point for $R =$ (i) 150, (j) 200, (k) 250, and (l) 300 nm. The best fits are displayed as dash lines.

p-pol	150 nm	200 nm	250 nm	300 nm
δ (meV)	$-0.30 - 0.10i$	$-1.66 - 0.48i$	$-5.56 + 1.67i$	$-3.2 + 1.01i$
τ (meV)	$-4.10 + 1.13i$	$-7.37 + 2.98i$	-2.10	$-0.28 - 0.32i$
$\tilde{\omega}_-$ (eV)	$1.771 + 0.0099i$	$1.770 + 0.011i$	$1.73 + 0.0177i$	$1.63 + 0.0114i$
$\tilde{\omega}_+$ (eV)	$1.8198 + 0.0025i$	$1.8011 + 0.0064i$	$1.772 + 0.0084i$	$1.7383 + 0.0081i$
d	-1	-1	1	1
s-pol	150 nm	200 nm	250 nm	300 nm
μ (meV)	-0.10	$-3.08 + 0.6i$	$-12.82 - 1.36i$	$-17.40 + 6.47i$
ε (meV)	$-12.47 + 0.89i$	$-29.85 + 5.08i$	$-19.48 + 4.04i$	$-14.23 - 7.35i$
$\tilde{\omega}_-$ (eV)	$1.725 + 0.0205i$	$1.7172 + 0.035i$	$1.737 + 0.021i$	$1.716 + 0.0305i$
$\tilde{\omega}_+$ (eV)	$1.792 + 0.006i$	$1.766 + 0.016i$	$1.771 + 0.026i$	$1.833 + 0.017i$
d	-1	-1	1	1

Table 1. The best fitted parameters for $R = 150, 200, 250$ and 300 nm

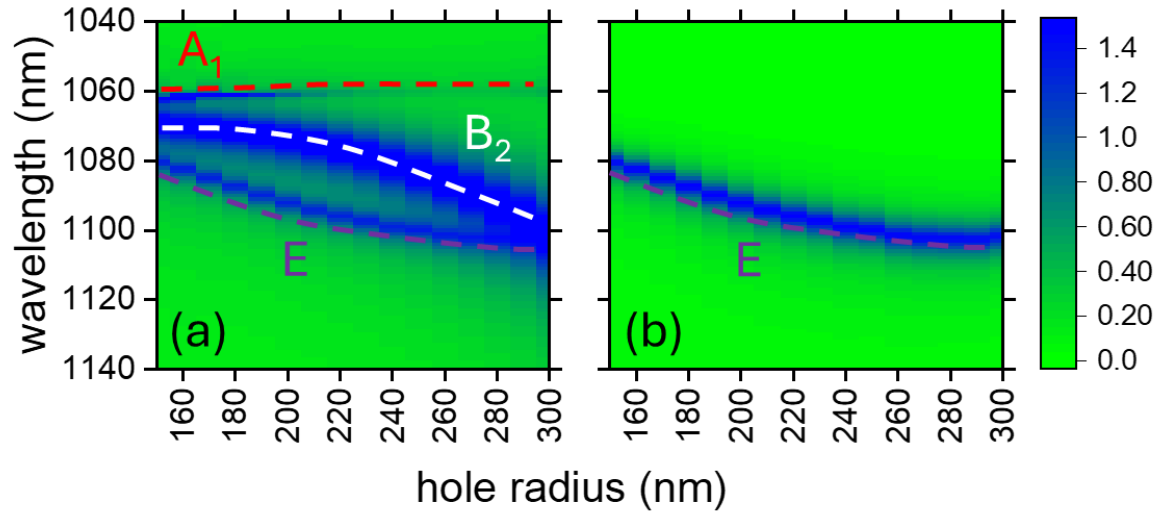


Fig. 5. The plots of the FDTD simulated (a) p- and (b) s-polarized radiation spectral mappings taken at the M point as a function of R . The color dash lines are for the visualization of the A_1 , B_2 , and E assignments.

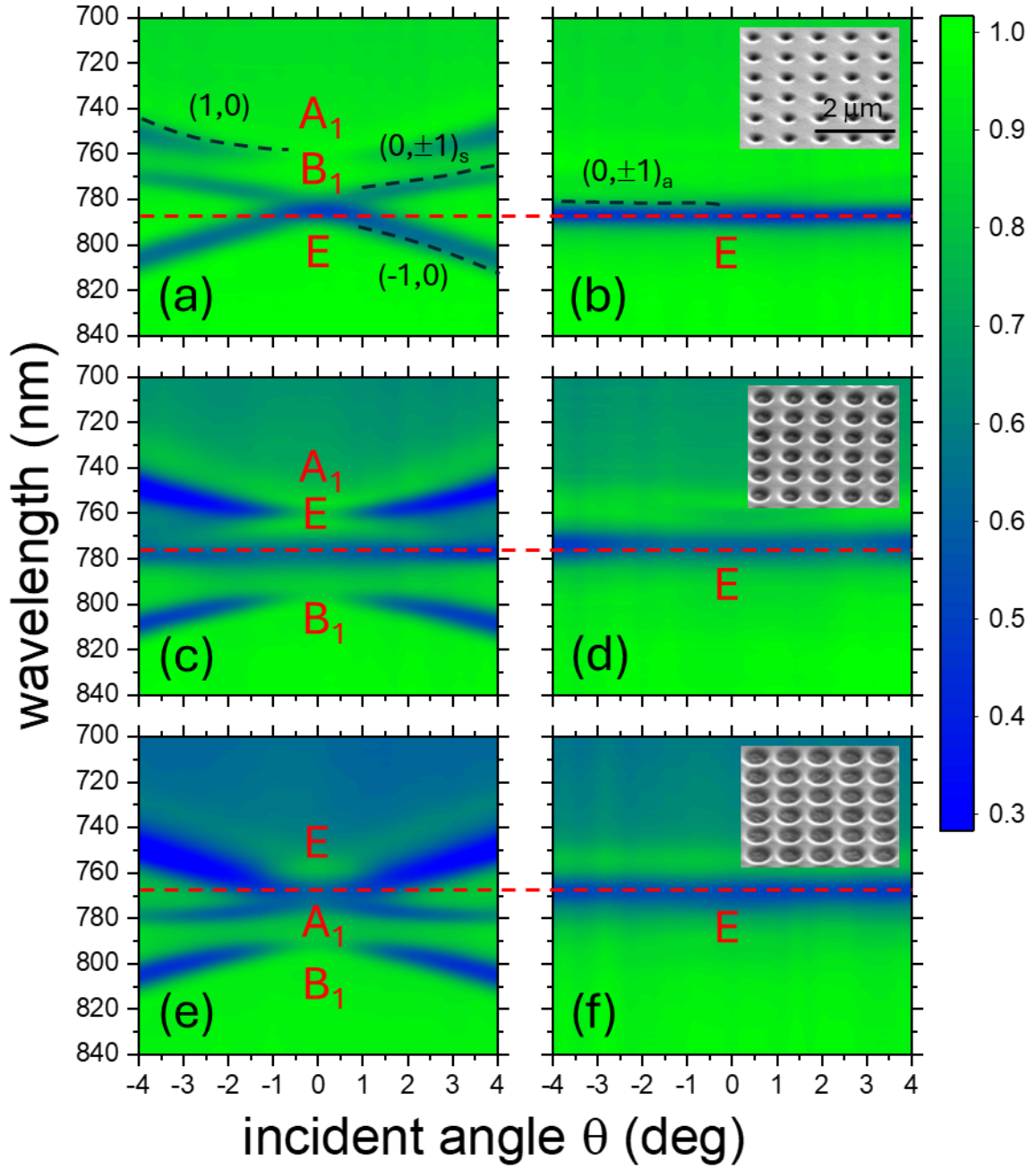


Fig. 6. The p-polarized angle-resolved specular reflectivity mappings measured near the Γ point along the Γ -X direction for $R =$ (a) 150, (c) 250 and (e) 300 nm. A_1 , B_1 and E are labelled at the Γ point. The s-polarized angle-resolved specular reflectivity mappings measured along the Γ -X direction for $R =$ (b) 150, (d) 250 and (f) 300 nm. E is labelled at the Γ point. The dispersion relations are sketched as dash lines. The red dash lines are displayed for E mode degeneracy. Insets: the corresponding SEM images.

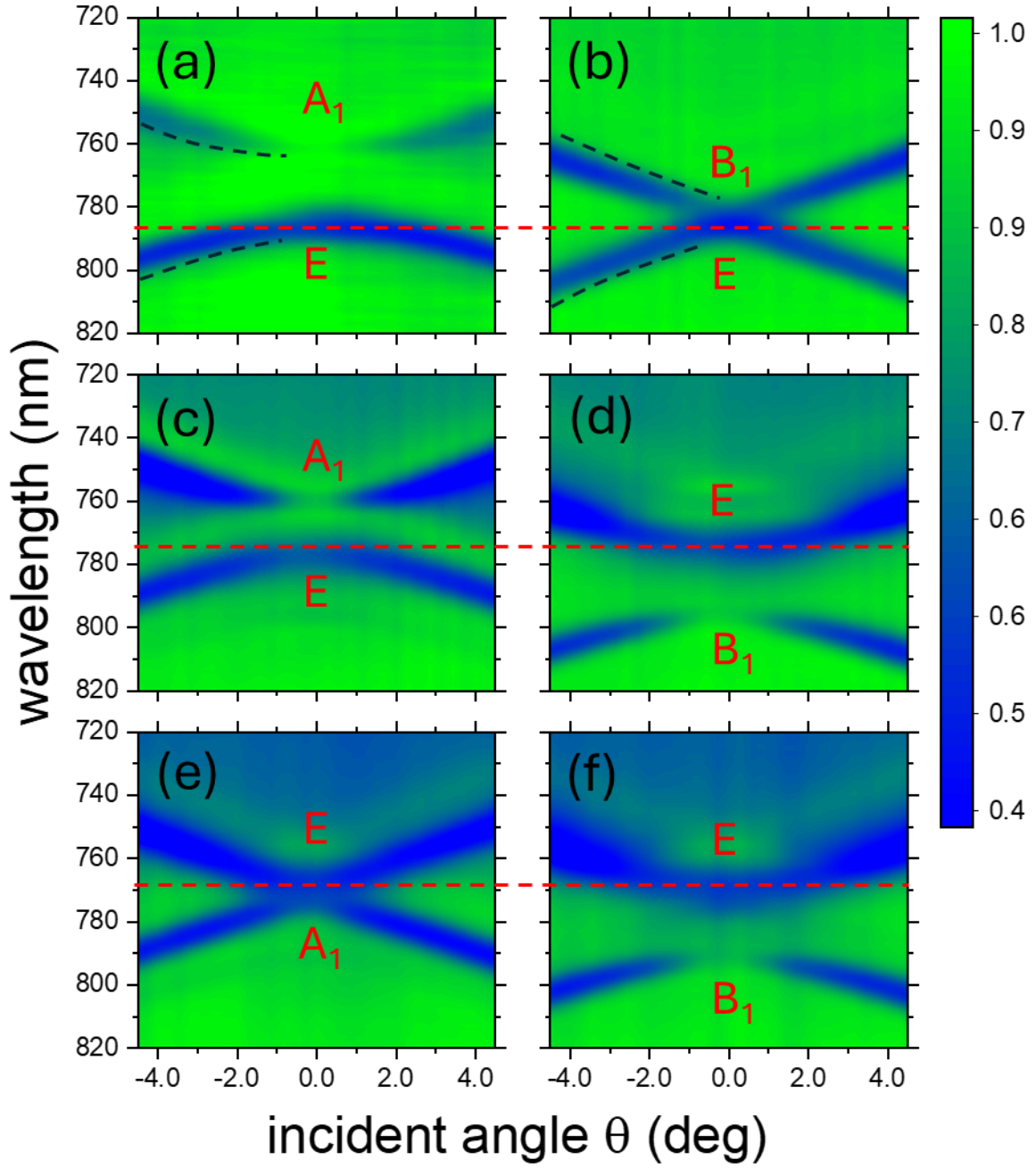


Fig. 7. The p-polarized angle-resolved specular reflectivity mappings measured near the Γ point along the Γ -M direction for $R =$ (a) 150, (c) 250 and (e) 300 nm. A_1 and E are labelled at the Γ point. The s-polarized angle-resolved specular reflectivity mappings measured along the Γ -M direction for $R =$ (b) 150, (d) 250 and (f) 300 nm. B_1 and E are labelled at the Γ point. The dispersion relations are sketched as dash lines. The red dash lines are displayed for E mode degeneracy.

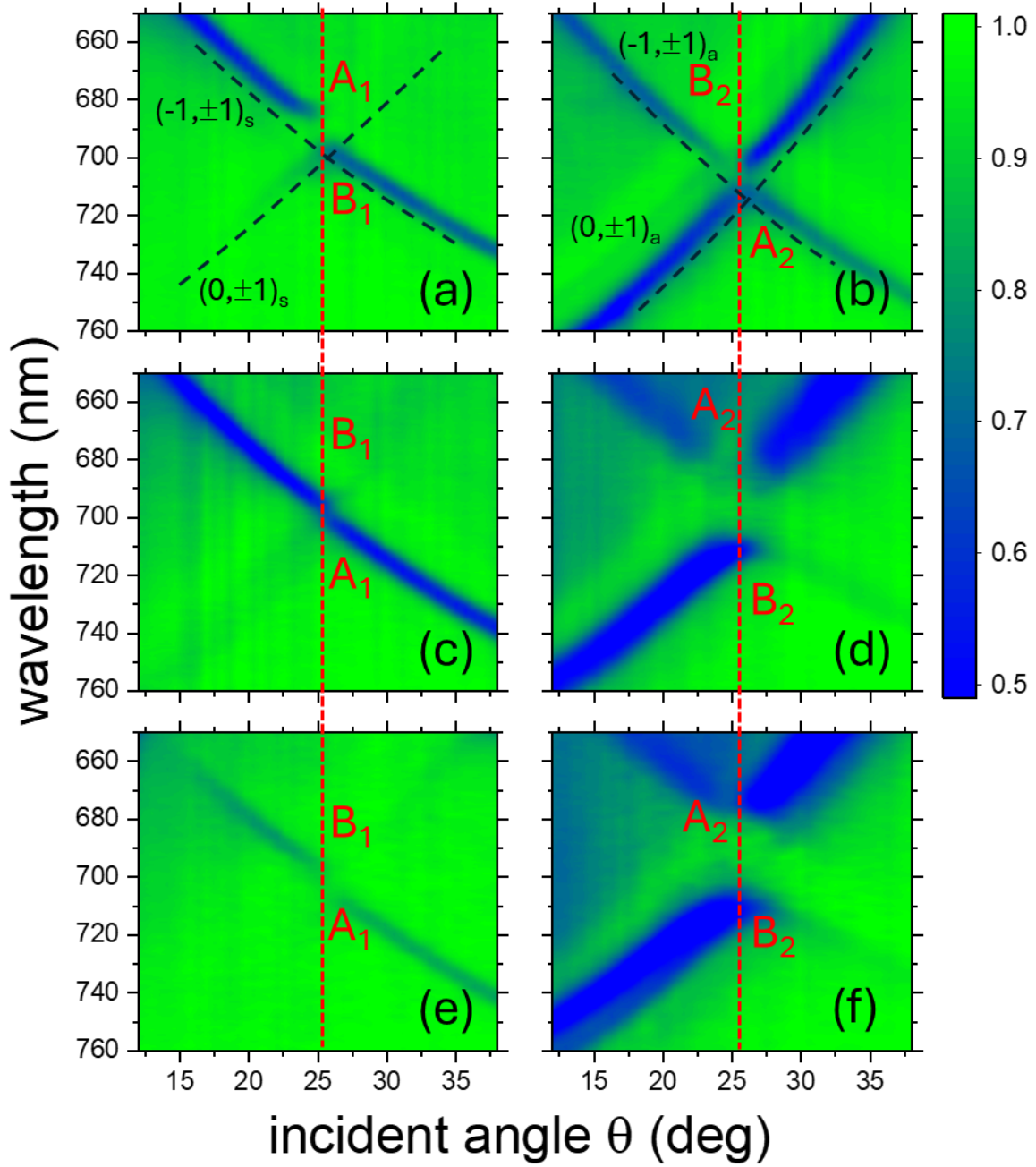


Fig. 8. The p-polarized angle-resolved specular reflectivity mappings measured near the X point along the Γ -X direction for $R =$ (a) 150, (c) 250 and (e) 300 nm. A_1 and B_1 are labelled at the X point. (a) The dispersion relations are displayed as dash lines. The s-polarized angle-resolved specular reflectivity mappings measured near the X point along the Γ -X direction for $R =$ (b) 150, (d) 250 and (f) 300 nm. A_2 and B_2 are labelled at the X point. (e) The dispersion relations are displayed as dash lines.

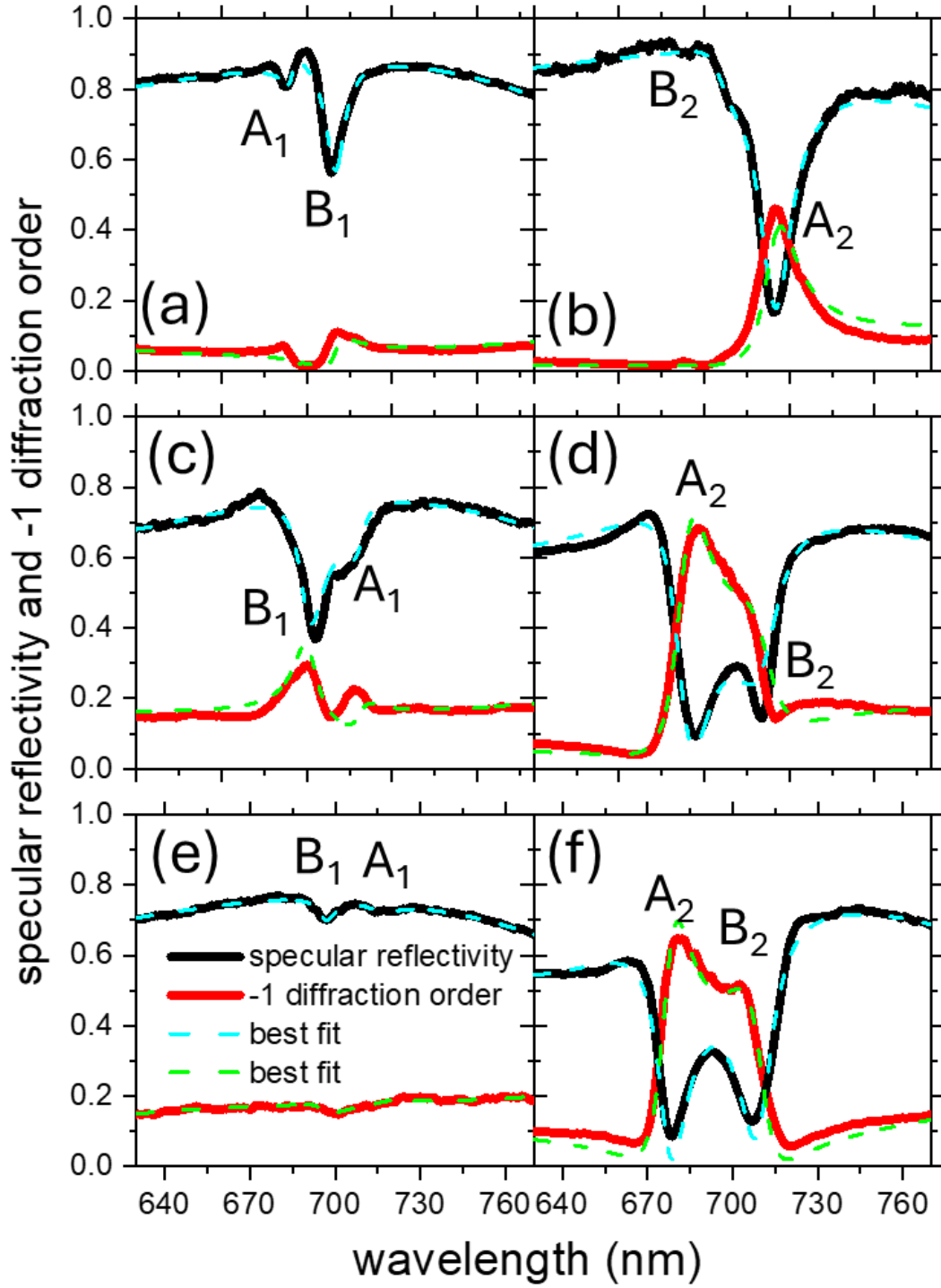


Fig. 9. The p-polarized specular reflectivity and -1st diffraction order spectra measured at the X point for $R =$ (a) 150, (c) 250, and (e) 300 nm. The best fits are displayed as dash lines. The s-polarized specular reflectivity and -1st diffraction order spectra measured at the X point for $R =$ (b) 150, (d) 250, and (f) 300 nm. The best fits are displayed as dash lines.

Table 2. The best fitted parameters for R = 150, 250 and 300 nm

p-pol	150 nm	250 nm	300 nm
δ (meV)	$-0.20i$	$-2.91 + 1.06i$	$-0.30 + 0.04i$
τ (meV)	$-1.9 - 0.02i$	$-0.55 - 0.58i$	$-0.29 + 0.07i$
$\tilde{\omega}_-$ (eV)	$1.771 + 0.01i$	$1.75 + 0.01i$	$1.73 + 0.0173i$
$\tilde{\omega}_+$ (eV)	$1.81 + 0.0044i$	$1.8 + 0.0137i$	$1.78 + 0.0095i$
d	-1	1	1
s-pol	150 nm	250 nm	300 nm
μ (meV)	$-8.4 + 1.1i$	$-6.6 - 2.1i$	$-9.9 - 1.4i$
ε (meV)	$-0.1 - 0.1i$	$-20.2 + 3.8i$	$-11.1 + 1.4i$
$\tilde{\omega}_-$ (eV)	$1.735 + 0.017i$	$1.743 + 0.023i$	$1.747 + 0.0184i$
$\tilde{\omega}_+$ (eV)	$1.77 + 0.0044i$	$1.815 + 0.019i$	$1.831 + 0.0173i$
d	-1	1	1

Supplementary Information

Determination of the irreducible representations at high symmetry points of two-dimensional square lattice plasmonic crystals by far-field radiations

T.H. Chan, Y.H. Guan, C. Liu, and H.C. Ong

Department of Physics, The Chinese University of Hong Kong, Shatin, Hong Kong, People's Republic of China

A. CMT formulation at the Γ point

As shown in Fig. S1(a), at the Γ point, four $(\pm 1, 0)$ and $(0, \pm 1)$ SPPs propagate in the $\pm x$ and $\pm y$ directions. The CMT equation, which carries the general form of $\frac{dA}{dt} = iHA + KS_+$, can be expressed as:

$$\frac{d}{dt} \begin{bmatrix} a_1 \\ a_2 \\ a_3 \\ a_4 \end{bmatrix} = i \begin{bmatrix} \tilde{\omega}_o & \alpha & \beta & \beta \\ \alpha & \tilde{\omega}_o & \beta & \beta \\ \beta & \beta & \tilde{\omega}_o & \alpha \\ \beta & \beta & \alpha & \tilde{\omega}_o \end{bmatrix} \begin{bmatrix} a_1 \\ a_2 \\ a_3 \\ a_4 \end{bmatrix} + \begin{bmatrix} \kappa & 0 \\ -\kappa & 0 \\ 0 & \kappa \\ 0 & -\kappa \end{bmatrix} \begin{bmatrix} s_{p+} \\ s_{s+} \end{bmatrix}, \quad (S1)$$

where A is a column vector with the mode amplitudes a_{1-4} , H is a symmetric matrix which contains the degenerate complex angular frequency $\tilde{\omega}_o = \omega_o + i(\Gamma_a + \Gamma_r)/2$, where Γ_a and Γ_r are the absorption and radiative decay rates, for a_{1-4} , and two complex interaction constants α and β . Because the Γ point possesses C_{4v} symmetry, the complex interaction constant is defined as α for the modes propagating in the same direction but β for the modes propagating in the perpendicular direction. They are complex provided both near- and far-field interactions are present. In addition, for the in-coupling matrix K and the incident power S_+ , each mode supports only one diffraction order with an in-coupling constant defined as κ , and the incident power amplitudes are defined as s_{p+} and s_{s+} for p- and s-polarizations in positive x and y directions. As shown in Fig. S1(b), the sign of κ depends on the relative orientation between the incident polarization and the transverse polarization of the SPP, which lies in the plane

defined by \vec{k}_{spp} . If they lie in the same direction, κ is positive, but it is negative when opposite.

Four diffraction orders will interfere and yield a specular (total) reflection.

Once Eq. (S1) is formulated, we then solve the eigenvalues and eigenvectors by performing diagonalization. By using transformation matrix T such that

$T \frac{dA}{dt} = iTHT^{-1}TA + TKS_+$, we have $\frac{d\tilde{A}}{dt} = i\tilde{H}\tilde{A} + \tilde{K}S_+$:

$$\frac{d}{dt} \begin{bmatrix} \tilde{a}_1 \\ \tilde{a}_2 \\ \tilde{a}_3 \\ \tilde{a}_4 \end{bmatrix} = i \begin{bmatrix} \tilde{\omega}_o - \alpha & 0 & 0 & 0 \\ 0 & \tilde{\omega}_o - \alpha & 0 & 0 \\ 0 & 0 & \tilde{\omega}_o + \alpha - 2\beta & 0 \\ 0 & 0 & 0 & \tilde{\omega}_o + \alpha + 2\beta \end{bmatrix} \begin{bmatrix} \tilde{a}_1 \\ \tilde{a}_2 \\ \tilde{a}_3 \\ \tilde{a}_4 \end{bmatrix} - \sqrt{2} \begin{bmatrix} 0 & \kappa \\ \kappa & 0 \\ 0 & 0 \\ 0 & 0 \end{bmatrix} \begin{bmatrix} s_{p+} \\ s_{s+} \end{bmatrix}, \quad (S2)$$

$$\text{where } T = \frac{1}{2} \begin{bmatrix} 0 & 0 & -\sqrt{2} & \sqrt{2} \\ -\sqrt{2} & \sqrt{2} & 0 & 0 \\ -1 & -1 & 1 & 1 \\ 1 & 1 & 1 & 1 \end{bmatrix} \text{ and } T^{-1} = T^T = \frac{1}{2} \begin{bmatrix} 0 & -\sqrt{2} & -1 & 1 \\ 0 & \sqrt{2} & -1 & 1 \\ -\sqrt{2} & 0 & 1 & 1 \\ \sqrt{2} & 0 & 1 & 1 \end{bmatrix}. \text{ From Eq.}$$

(S2), we see from \tilde{H} that $\tilde{a}_{1,2}$ modes are degenerate with $\tilde{\omega}_{1,2} = \tilde{\omega}_o - \alpha$ but $\tilde{a}_{3,4}$ modes,

$\tilde{\omega}_{3,4} = \tilde{\omega}_o + \alpha \mp 2\beta$, are nondegenerate. Assuming a_{1-4} have the spatial form of $e^{i\vec{k}_{spp} \cdot \vec{r}}$, or

$e^{\pm i \frac{2\pi}{P} x}$ and $e^{\pm i \frac{2\pi}{P} y}$, their electric field magnitudes in the z direction, $E_z(x, y)$, can be roughly

$$\text{approximated as: } \begin{bmatrix} \tilde{a}_1 \\ \tilde{a}_2 \\ \tilde{a}_3 \\ \tilde{a}_4 \end{bmatrix} = T \begin{bmatrix} a_1 \\ a_2 \\ a_3 \\ a_4 \end{bmatrix} = \begin{bmatrix} \frac{-a_3 + a_4}{\sqrt{2}} \\ \frac{-a_1 + a_2}{\sqrt{2}} \\ \frac{-a_1 - a_2 + a_3 + a_4}{2} \\ \frac{a_1 + a_2 + a_3 + a_4}{2} \end{bmatrix} = \begin{bmatrix} -\sqrt{2}i \sin(2\pi y/P) \\ -\sqrt{2}i \sin(2\pi x/P) \\ -\cos(2\pi x/P) + \cos(2\pi y/P) \\ \cos(2\pi x/P) + \cos(2\pi y/P) \end{bmatrix}.$$

Their field patterns are illustrated in the following Fig. S1(c), and they are assigned as E , B_1 and A_1 for $\tilde{a}_{1,2}$, \tilde{a}_3 , and \tilde{a}_4 .

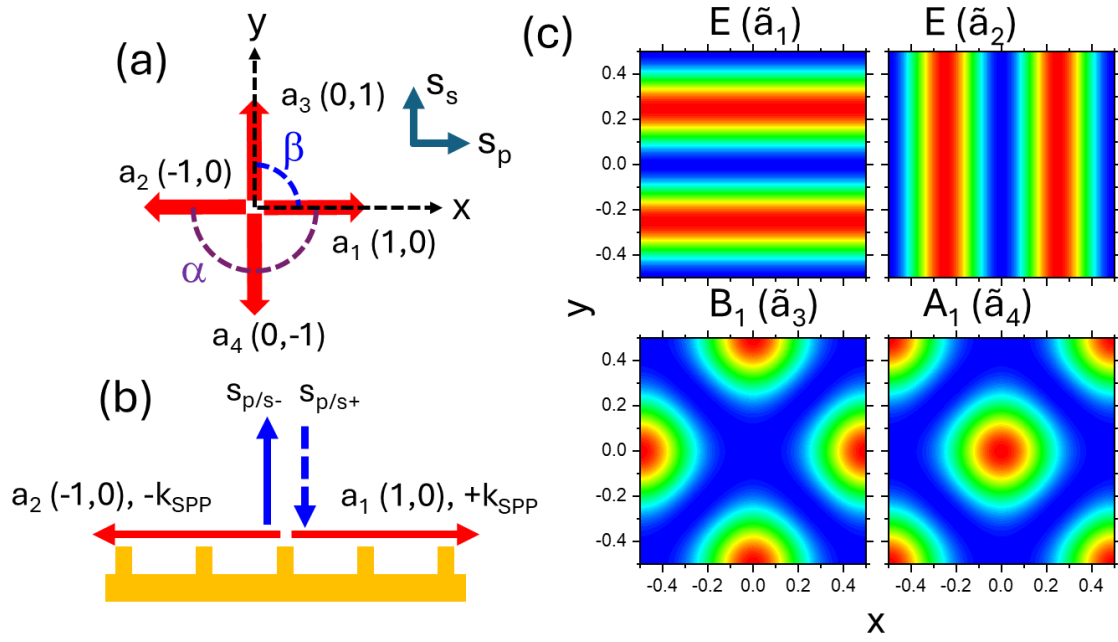


Fig. S1. (a) The schematic plane-view of how four $(\pm 1, 0)$ and $(0, \pm 1)$ SPPs couple at the Γ point for CMT formulation and the coupling constants are defined as α and β . (b) The cross-section view shows the incoming s_+ and the outgoing specular (total) reflectivity s_- channels at the Γ point. Each channel carries p- and s-polarizations. (c) The field patterns of \tilde{a}_{1-4} and are labelled as E , B_1 , and A_1 .

B. CMT formulation at the X point

As shown in S2(a), at the X point, four degenerate $(0, \pm 1)$ and $(-1, \pm 1)$ SPPs couple together and the CMT equation can be expressed as:

$$\frac{d}{dt} \begin{bmatrix} a_1 \\ a_2 \\ a_3 \\ a_4 \end{bmatrix} = i \begin{bmatrix} \tilde{\omega}_o & \sigma & \gamma & \eta \\ \sigma & \tilde{\omega}_o & \eta & \gamma \\ \gamma & \eta & \tilde{\omega}_o & \sigma \\ \eta & \gamma & \sigma & \tilde{\omega}_o \end{bmatrix} \begin{bmatrix} a_1 \\ a_2 \\ a_3 \\ a_4 \end{bmatrix} + \begin{bmatrix} -\kappa_{pL} & \kappa_{sL} & -\kappa_{pR} & \kappa_{sR} \\ \kappa_{pR} & -\kappa_{sR} & \kappa_{pL} & -\kappa_{sL} \\ -\kappa_{pL} & -\kappa_{sL} & -\kappa_{pR} & -\kappa_{sR} \\ \kappa_{pR} & \kappa_{sR} & \kappa_{pL} & \kappa_{sL} \end{bmatrix} \begin{bmatrix} s_{pL+} \\ s_{sL+} \\ s_{pR+} \\ s_{sR+} \end{bmatrix}, \quad (\text{S3})$$

where the complex coupling constants are η , γ , and σ for the modes oriented relatively to each other by 60° , 120° , and 180° , respectively. As the X point follows C_{2v} symmetry in which only two right- and left-hand diffractions are supported, the in-coupling matrix K has right and left input channels and each channel carries p- and s-polarizations, as shown in Fig. S2(b). The first p/s and second R/L subscripts for κ and s_+ in K and S_+ in Eq. (S3) define the p/s polarizations and the right/left incidences.

After diagonalization, Eq. (S3) is transformed as:

$$\frac{d}{dt} \begin{bmatrix} \tilde{a}_1 \\ \tilde{a}_2 \\ \tilde{a}_3 \\ \tilde{a}_4 \end{bmatrix} = i \begin{bmatrix} \tilde{\omega}_o + \sigma - \gamma - \eta & 0 & 0 & 0 \\ 0 & \tilde{\omega}_o - \sigma + \gamma - \eta & 0 & 0 \\ 0 & 0 & \tilde{\omega}_o - \sigma - \gamma + \eta & 0 \\ 0 & 0 & 0 & \tilde{\omega}_o + \sigma + \gamma + \eta \end{bmatrix} \begin{bmatrix} \tilde{a}_1 \\ \tilde{a}_2 \\ \tilde{a}_3 \\ \tilde{a}_4 \end{bmatrix} + TK \begin{bmatrix} s_{pL+} \\ s_{sL+} \\ s_{pR+} \\ s_{sR+} \end{bmatrix}, \quad (\text{S4})$$

where the transformation matrices T and $T^{-1} = T^T$ are $\frac{1}{2} \begin{bmatrix} -1 & -1 & 1 & 1 \\ -1 & 1 & -1 & 1 \\ 1 & -1 & -1 & 1 \\ 1 & 1 & 1 & 1 \end{bmatrix}$ and

$\frac{1}{2} \begin{bmatrix} -1 & -1 & 1 & 1 \\ -1 & 1 & -1 & 1 \\ 1 & -1 & -1 & 1 \\ 1 & 1 & 1 & 1 \end{bmatrix}$, respectively. We see all the coupled modes are nondegenerate. As a

$$\text{result, } TKS_+ = \begin{bmatrix} 0 & \kappa_{sR} - \kappa_{sL} & 0 & -(\kappa_{sR} - \kappa_{sL}) \\ \kappa_{pR} + \kappa_{pL} & 0 & \kappa_{pR} + \kappa_{pL} & 0 \\ 0 & \kappa_{sR} + \kappa_{sL} & 0 & \kappa_{sR} + \kappa_{sL} \\ \kappa_{pR} - \kappa_{pL} & 0 & -(\kappa_{pR} - \kappa_{pL}) & 0 \end{bmatrix} \begin{bmatrix} s_{pL+} \\ s_{sL+} \\ s_{pR+} \\ s_{sR+} \end{bmatrix}, \text{ which is equal to}$$

$$\begin{bmatrix} (\kappa_{sR} - \kappa_{sL})s_{sL+} - (\kappa_{sR} - \kappa_{sL})s_{sR+} \\ (\kappa_{pR} + \kappa_{pL})s_{pL+} + (\kappa_{pR} + \kappa_{pL})s_{pR+} \\ (\kappa_{sR} + \kappa_{sL})s_{sL+} + (\kappa_{sR} + \kappa_{sL})s_{sR+} \\ (\kappa_{pR} - \kappa_{pL})s_{pL+} - (\kappa_{pR} - \kappa_{pL})s_{pR+} \end{bmatrix}, \quad \text{and} \quad \begin{bmatrix} \tilde{a}_1 \\ \tilde{a}_2 \\ \tilde{a}_3 \\ \tilde{a}_4 \end{bmatrix} = \frac{1}{2} \begin{bmatrix} -a_1 - a_2 + a_3 + a_4 \\ -a_1 + a_2 - a_3 + a_4 \\ a_1 - a_2 - a_3 + a_4 \\ a_1 + a_2 + a_3 + a_4 \end{bmatrix} = \\
= 2 \begin{bmatrix} -\sin(\pi x/P) \sin(2\pi y/P) \\ i \sin(\pi x/P) \cos(2\pi y/P) \\ i \cos(\pi x/P) \sin(2\pi y/P) \\ \cos(\pi x/P) \cos(2\pi y/P) \end{bmatrix}, \text{ assuming } a_{1-4} \text{ have the spatial form of } e^{i\vec{k}_{spp} \cdot \vec{r}}, \text{ or } e^{\pm i(x \pm 2y)(\pi/P)}.$$

From Eq. (S4), we see $\tilde{a}_1 = \frac{(\kappa_{sR} - \kappa_{sL})(s_{sL+} - s_{sR+})}{i(\omega - \tilde{\omega}_1)}$, $\tilde{a}_2 = \frac{(\kappa_{pR} + \kappa_{pL})(s_{pL+} + s_{pR+})}{i(\omega - \tilde{\omega}_2)}$,

$\tilde{a}_3 = \frac{(\kappa_{sR} + \kappa_{sL})(s_{sL+} + s_{sR+})}{i(\omega - \tilde{\omega}_3)}$, and $\tilde{a}_4 = \frac{(\kappa_{pR} - \kappa_{pL})(s_{pL+} - s_{pR+})}{i(\omega - \tilde{\omega}_4)}$. The corresponding field

patterns are illustrated in Fig. S2(c) and \tilde{a}_1 and \tilde{a}_3 are assigned to be B_2 and A_2 where \tilde{a}_2 and \tilde{a}_4 are assigned to be B_1 and A_1 .

We then formulate their right and left diffraction orders. We define the specular reflection and the -1st diffraction order as follows. As shown in Fig. S2(b), if the incidence is the right incoming channel ($s_{s/pR+}$), then the specular reflection and the -1st diffraction orders are the left ($s_{s/pL-}$) and right ($s_{s/pR-}$) outgoing channels. Therefore, by using conservation of energy and time reversal symmetry, the outgoing radiation channels are expressed as

$$S_- = CS_+ + K^T T^T \tilde{A} \text{ or}$$

$$\begin{bmatrix} s_{pL-} \\ s_{sL-} \\ s_{pR-} \\ s_{sR-} \end{bmatrix} = C \begin{bmatrix} s_{pL+} \\ s_{sL+} \\ s_{pR+} \\ s_{sR+} \end{bmatrix} + K^T T^T \begin{bmatrix} \tilde{a}_1 \\ \tilde{a}_2 \\ \tilde{a}_3 \\ \tilde{a}_4 \end{bmatrix}, \quad (S5)$$

where C is the non-resonant scattering matrix and

$$K^T T^T = \frac{1}{2} \begin{bmatrix} -\kappa_{pL} & \kappa_{pR} & -\kappa_{pL} & \kappa_{pR} \\ \kappa_{sL} & -\kappa_{sR} & -\kappa_{sL} & \kappa_{sR} \\ -\kappa_{pR} & \kappa_{pL} & -\kappa_{pR} & \kappa_{pL} \\ \kappa_{sR} & -\kappa_{sL} & -\kappa_{sR} & \kappa_{sL} \end{bmatrix} \begin{bmatrix} -1 & -1 & 1 & 1 \\ -1 & 1 & -1 & 1 \\ 1 & -1 & -1 & 1 \\ 1 & 1 & 1 & 1 \end{bmatrix} = \\
\begin{bmatrix} 0 & \kappa_{pR} + \kappa_{pL} & 0 & \kappa_{pR} - \kappa_{pL} \\ \kappa_{sR} - \kappa_{sL} & 0 & \kappa_{sR} + \kappa_{sL} & 0 \\ 0 & \kappa_{pR} + \kappa_{pL} & 0 & -(\kappa_{pR} - \kappa_{pL}) \\ -(\kappa_{sR} - \kappa_{sL}) & 0 & \kappa_{sR} + \kappa_{sL} & 0 \end{bmatrix}. \text{ As a result, Eq. (S5) becomes:}$$

$$\begin{bmatrix} s_{pL-} \\ s_{sL-} \\ s_{pR-} \\ s_{sR-} \end{bmatrix} = C \begin{bmatrix} s_{pL+} \\ s_{sL+} \\ s_{pR+} \\ s_{sR+} \end{bmatrix} + \begin{bmatrix} 0 \\ \kappa_{sR} - \kappa_{sL} \\ 0 \\ -(\kappa_{sR} - \kappa_{sL}) \end{bmatrix} \tilde{a}_1 + \begin{bmatrix} \kappa_{pR} + \kappa_{pL} \\ 0 \\ \kappa_{pR} + \kappa_{pL} \\ 0 \end{bmatrix} \tilde{a}_2 + \begin{bmatrix} 0 \\ \kappa_{sR} + \kappa_{sL} \\ 0 \\ \kappa_{sR} + \kappa_{sL} \end{bmatrix} \tilde{a}_3 + \begin{bmatrix} \kappa_{pR} - \kappa_{pL} \\ 0 \\ -(\kappa_{pR} - \kappa_{pL}) \\ 0 \end{bmatrix} \tilde{a}_4, \quad (S6)$$

By taking only $s_{sR+} \neq 0$ under single right s-incidence, the diffraction orders are:

$$\begin{bmatrix} s_{pL-} \\ s_{sL-} \\ s_{pR-} \\ s_{sR-} \end{bmatrix} = C \begin{bmatrix} 0 \\ 0 \\ 0 \\ s_{sR+} \end{bmatrix} + \begin{bmatrix} 0 \\ -(\kappa_{sR} - \kappa_{sL})^2 \\ 0 \\ (\kappa_{sR} - \kappa_{sL})^2 \end{bmatrix} \frac{s_{sR+}}{i(\omega - \tilde{\omega}_1)} + \begin{bmatrix} 0 \\ (\kappa_{sR} + \kappa_{sL})^2 \\ 0 \\ (\kappa_{sR} + \kappa_{sL})^2 \end{bmatrix} \frac{s_{sR+}}{i(\omega - \tilde{\omega}_3)}, \quad (S7)$$

showing only two diffractions at $\tilde{\omega}_1$ (B₂) and $\tilde{\omega}_3$ (A₂) are present and they both are s-polarized. In addition, while the left (specular reflectivity) and right (-1 diffraction order) diffractions from A₂ are in phase, those from B₂ are π out of phase. Likewise, for $s_{pR+} \neq 0$, we have

$$\begin{bmatrix} s_{pL-} \\ s_{sL-} \\ s_{pR-} \\ s_{sR-} \end{bmatrix} = C \begin{bmatrix} 0 \\ 0 \\ s_{pR+} \\ 0 \end{bmatrix} + \begin{bmatrix} (\kappa_{pR} + \kappa_{pL})^2 \\ 0 \\ (\kappa_{pR} + \kappa_{pL})^2 \\ 0 \end{bmatrix} \frac{s_{pR+}}{i(\omega - \tilde{\omega}_2)} + \begin{bmatrix} -(\kappa_{pR} - \kappa_{pL})^2 \\ 0 \\ (\kappa_{pR} - \kappa_{pL})^2 \\ 0 \end{bmatrix} \frac{s_{pR+}}{i(\omega - \tilde{\omega}_4)}, \quad (S8)$$

indicating only p-polarized diffractions at $\tilde{\omega}_2$ (B₁) and $\tilde{\omega}_4$ (A₁) exist. The left (specular reflectivity) and right (-1 diffraction order) diffractions are in phase for B₁ but π out of phase for A₁.

Eq. (S7) and (S8) can be further simplified. We rewrite them for the Frensel $r_{p/s,0}$ and $r_{p/s,-1}$ coefficients as two superimposed Lorentzian profiles given as:

$$\begin{bmatrix} r_{p,0} \\ r_{p,-1} \end{bmatrix} = \begin{bmatrix} p_{0,b} \\ p_{-1,b} e^{i\frac{\pi}{2}} \end{bmatrix} + \begin{bmatrix} \frac{(\kappa_{pR} + \kappa_{pL})^2}{i(\omega - \tilde{\omega}_2)} - \frac{(\kappa_{pR} - \kappa_{pL})^2}{i(\omega - \tilde{\omega}_4)} \\ \frac{(\kappa_{pR} + \kappa_{pL})^2}{i(\omega - \tilde{\omega}_2)} + \frac{(\kappa_{pR} - \kappa_{pL})^2}{i(\omega - \tilde{\omega}_4)} \end{bmatrix} = \begin{bmatrix} p_{0,b} \\ ip_{-1,b} \end{bmatrix} + \begin{bmatrix} \frac{\delta}{i(\omega - \tilde{\omega}_2)} - \frac{\gamma}{i(\omega - \tilde{\omega}_4)} \\ \frac{\delta}{i(\omega - \tilde{\omega}_2)} + \frac{\gamma}{i(\omega - \tilde{\omega}_4)} \end{bmatrix} \text{ or} \quad (S9)$$

$$\begin{bmatrix} r_{p,0} \\ r_{p,-1} \end{bmatrix} = \begin{bmatrix} p_{0,b} \\ ip_{-1,b} \end{bmatrix} + \begin{bmatrix} \frac{\delta}{i(\omega - \tilde{\omega}_+)} - \frac{\gamma}{i(\omega - \tilde{\omega}_-)} \\ d \left(\frac{\delta}{i(\omega - \tilde{\omega}_+)} + \frac{\gamma}{i(\omega - \tilde{\omega}_-)} \right) \end{bmatrix},$$

and

$$\begin{aligned}
\begin{bmatrix} r_{s,0} \\ r_{s,-1} \end{bmatrix} &= \begin{bmatrix} s_{0,b} \\ s_{-1,b} e^{i\frac{\pi}{2}} \end{bmatrix} + \begin{bmatrix} \frac{-(\kappa_{sR} - \kappa_{sL})^2}{i(\omega - \tilde{\omega}_1)} + \frac{(\kappa_{sR} + \kappa_{sL})^2}{i(\omega - \tilde{\omega}_3)} \\ \frac{(\kappa_{sR} - \kappa_{sL})^2}{i(\omega - \tilde{\omega}_1)} + \frac{(\kappa_{sR} + \kappa_{sL})^2}{i(\omega - \tilde{\omega}_3)} \end{bmatrix} \text{ or} \\
\begin{bmatrix} r_{s,0} \\ r_{s,-1} \end{bmatrix} &= \begin{bmatrix} s_{0,b} \\ i s_{-1,b} \end{bmatrix} + \begin{bmatrix} \frac{\mu}{i(\omega - \tilde{\omega}_+)} + \frac{\varepsilon}{i(\omega - \tilde{\omega}_-)} \\ d \left(\frac{\mu}{i(\omega - \tilde{\omega}_+)} - \frac{\varepsilon}{i(\omega - \tilde{\omega}_-)} \right) \end{bmatrix}, \tag{S10}
\end{aligned}$$

where $p/s_{0,b}$ and $p/s_{-1,b}$ are the nonresonant backgrounds, $\tilde{\omega}_-$ and $\tilde{\omega}_+$ are the complex angular frequencies for the coupled modes, and δ , γ , μ , and ε are the constants. The phase differences between $p/s_{0,b}$ and $p/s_{-1,b}$ are known to be $-\pi/2$ [1,2]. The symmetry factor d is either 1 or -1, which determines whether $\tilde{\omega}_+$ is A_1 or B_1 under p-polarization and A_2 or B_2 under s-polarization. We can fit the specular reflectivity and -1 diffraction order spectra by using $|r_{p/s,0}|^2$ and $|r_{p/s,-1}|^2$ from Eq. (S9) & (S10). For p-polarization, if $d = 1$, it indicates $\tilde{\omega}_+$ is $\tilde{\omega}_2$ (B_1) but is $\tilde{\omega}_4$ (A_1) if $d = -1$. On the other hand, for s-polarization, $\tilde{\omega}_+$ is $\tilde{\omega}_3$ (A_2) for $d = 1$ but $\tilde{\omega}_1$ (B_2) for $d = -1$.

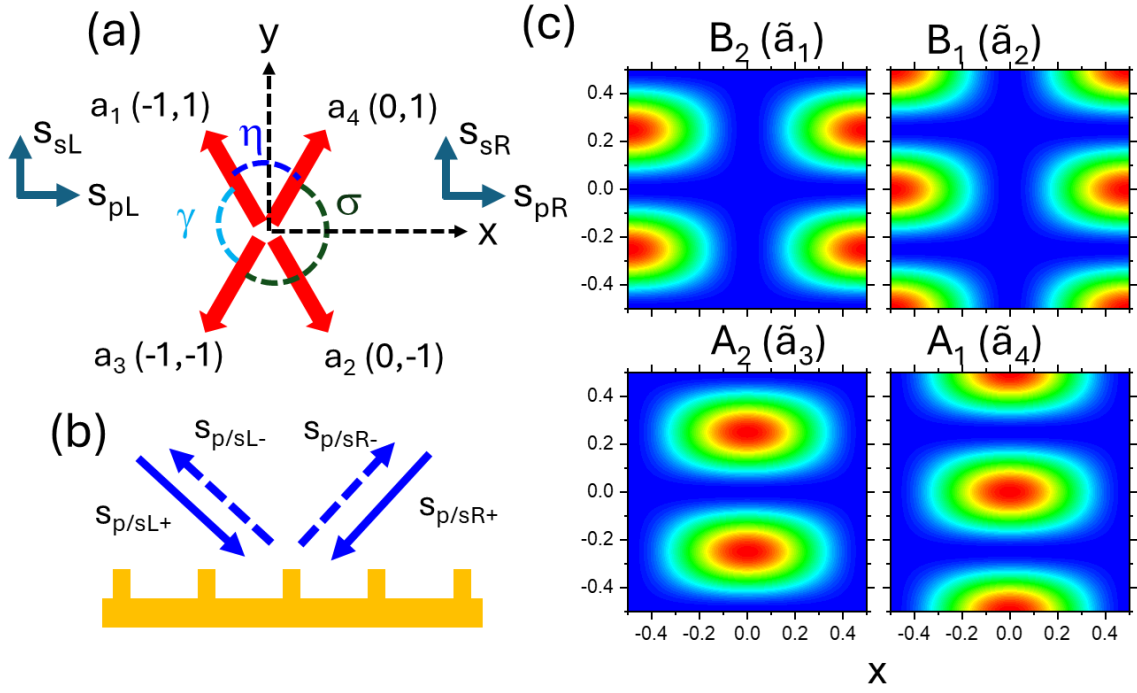


Fig. S2. (a) The schematic plane-view of how four $(0,\pm 1)$ and $(-1,\pm 1)$ SPPs couple at the X point for CMT formulation and the coupling constants are defined as η , γ , and σ . (b) The cross-section view shows the left and right incoming s_+ and the outgoing s_- channels at the X point. Each channel carries p- and s-polarizations. If the right incoming channel is the incidence, then the left and right outgoing channels are the specular reflection and -1 diffraction order, respectively. (c) The field patterns of \tilde{a}_{1-4} and are labelled as B_2 , B_1 , A_2 and A_1 .

C. FDTD results at the Γ point

Fig. S3(a)-(d) show the p- and s-polarized total reflectivity spectral mappings taken along the Γ -X direction, i.e. $\varphi = 0^\circ$, at $\theta = 0^\circ$ and 1° for different R. Fig. S4-7(a)-(c) show the reflectivity spectra taken at $\theta = 0^\circ$ and 1° and their corresponding field patterns for R = 150, 200, 250, and 300 nm.

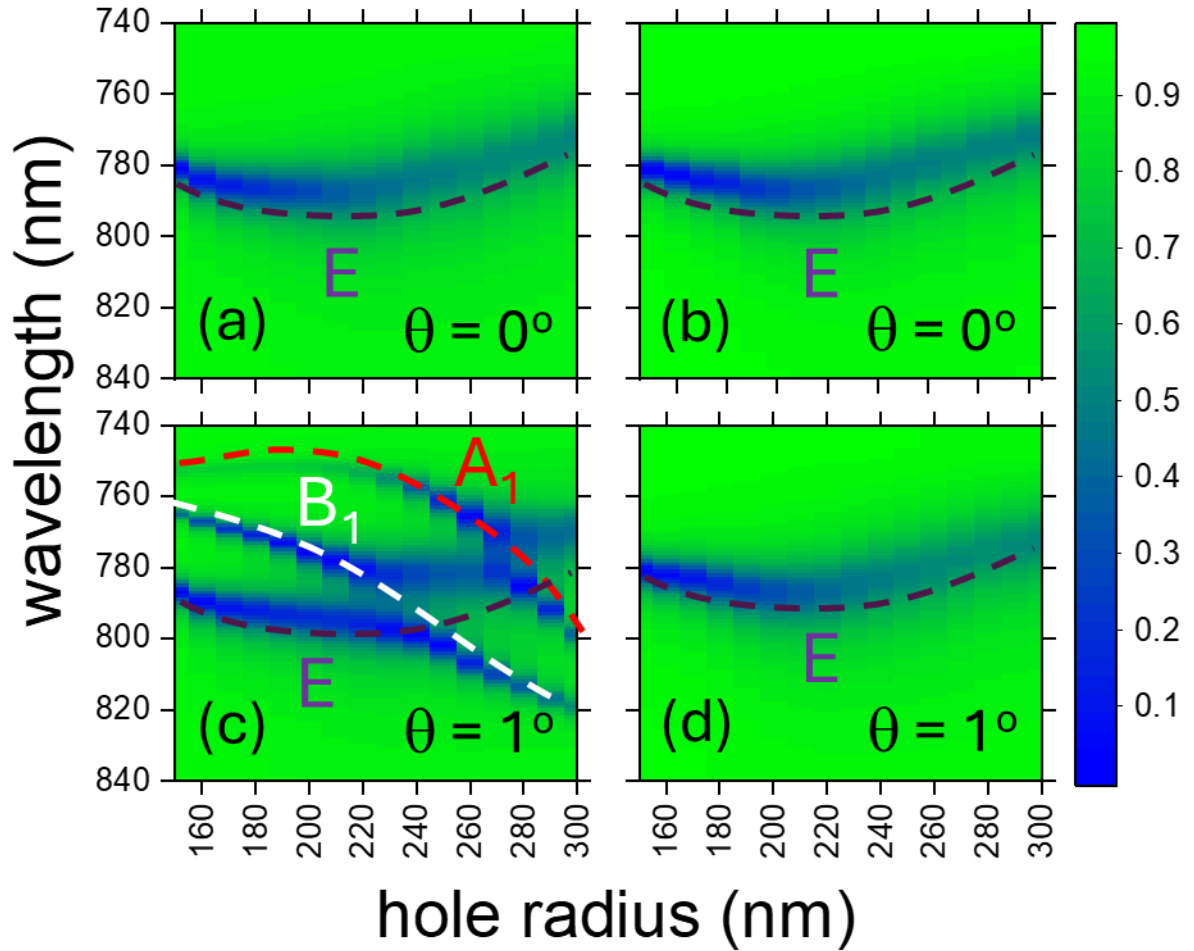


Fig. S3. The p-polarized total reflectivity spectral mappings taken along the Γ -X direction, i.e. $\varphi = 0^\circ$, at $\theta =$ (a) 0° and (c) 1° for different R. The s-polarized total reflectivity spectral mappings taken along the Γ -X direction, i.e. $\varphi = 0^\circ$, at $\theta =$ (b) 0° and (d) 1° for different R. The dash lines are the A_1 , B_1 , and E modes for visualization.

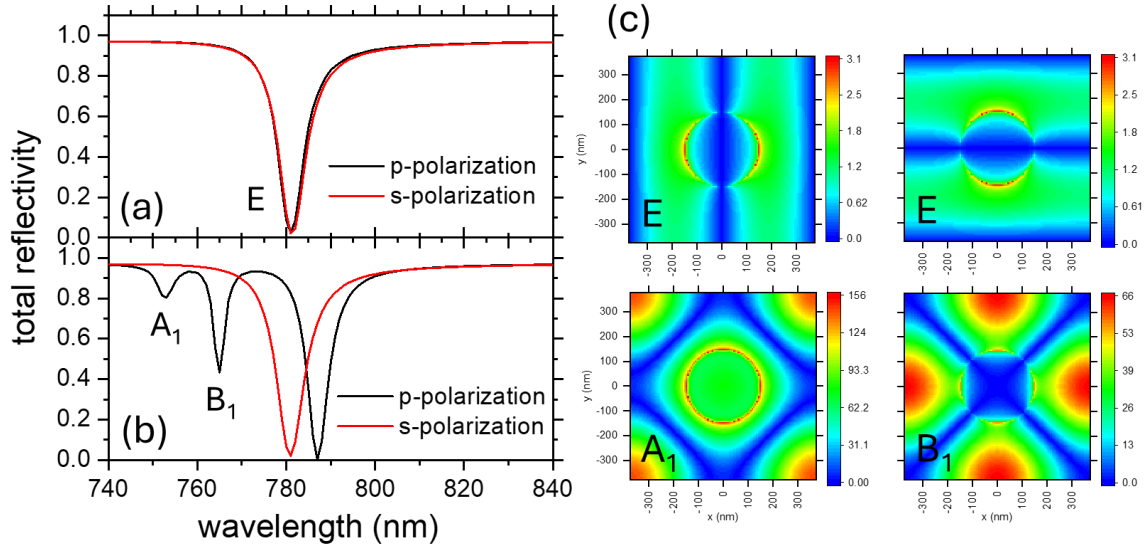


Fig. S4. For $R = 150$ nm, the (a) p- and s-polarized reflectivity spectra taken at the Γ point. The (b) p- and s-polarized reflectivity spectra taken at $\theta = 1^\circ$. (c) The corresponding electric near-field patterns taken at $\lambda =$ (a) 781 nm are labelled as E and (b) = 752 and 765 nm are labelled as A_1 and B_1 .

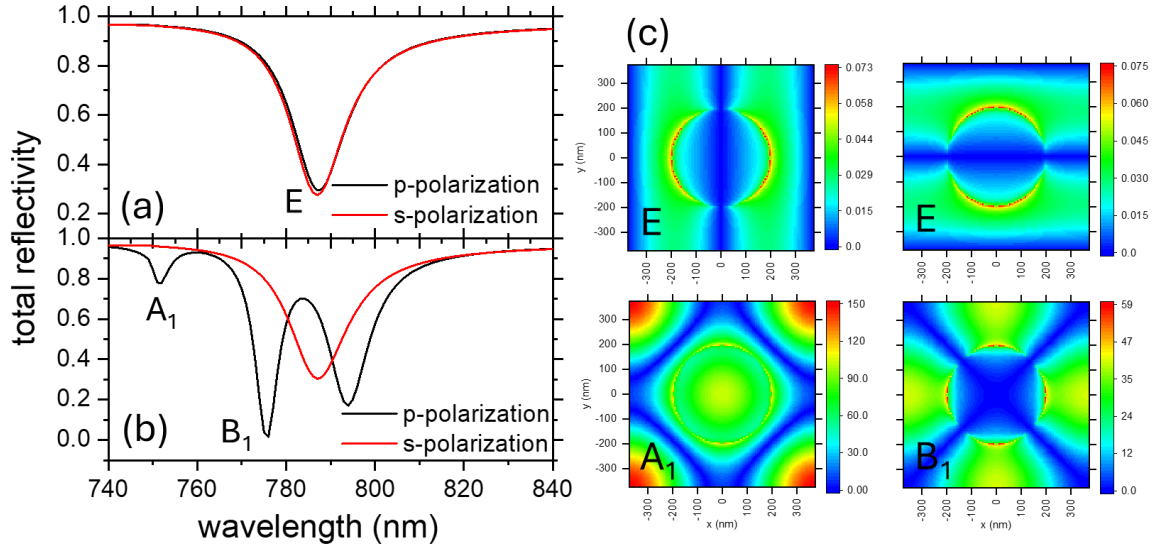


Fig. S5. For $R = 200$ nm, the (a) p- and s-polarized reflectivity spectra taken at the Γ point. The (b) p- and s-polarized reflectivity spectra taken at $\theta = 1^\circ$. (c) The corresponding electric near-field patterns taken at $\lambda =$ (a) 787 nm are labelled as E and (b) = 751 and 776 nm are labelled as A_1 and B_1 .

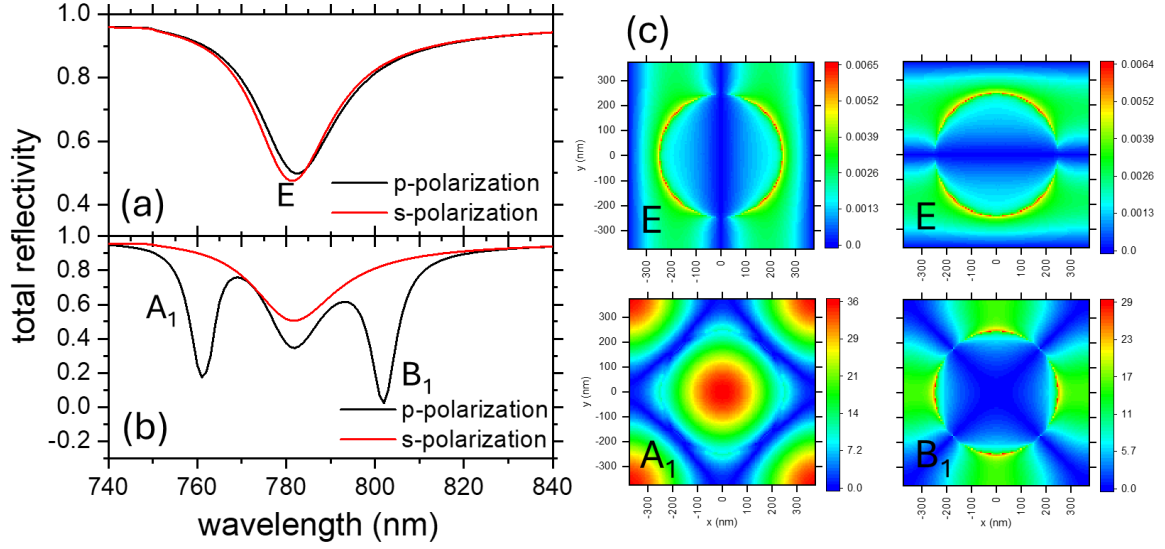


Fig. S6. For $R = 250$ nm, the (a) p- and s-polarized reflectivity spectra taken at the Γ point. The (b) p- and s-polarized reflectivity spectra taken at $\theta = 1^\circ$. (c) The corresponding electric near-field patterns taken at $\lambda =$ (a) 782 nm are labelled as E and (b) = 761 and 802 nm are labelled as A_1 and B_1 .

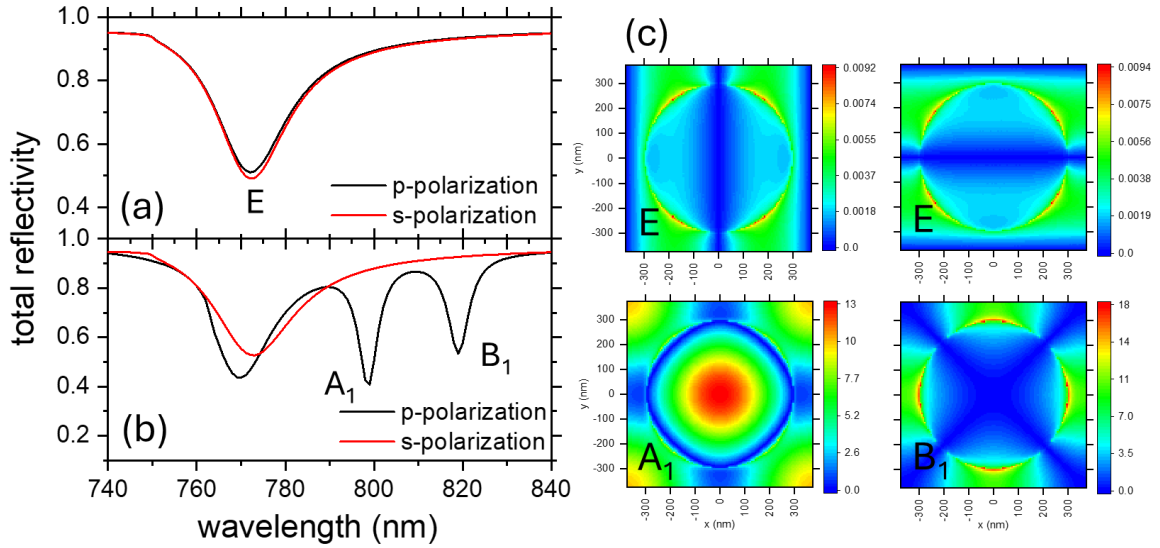


Fig. S7. For $R = 300$ nm, the (a) p- and s-polarized reflectivity spectra taken at the Γ point. The (b) p- and s-polarized reflectivity spectra taken at $\theta = 1^\circ$. (c) The corresponding electric near-field patterns taken at $\lambda =$ (a) 772 nm are labelled as E and (b) = 798 and 819 nm are labelled as A_1 and B_1 .

D. FDTD results at the X point

Fig. S8(a) & (b) show the p- and s-polarized total reflectivity spectral mappings the X point for different R. Fig. S9-12(a) & (b) show the reflectivity spectra and the corresponding field patterns taken at the X point for R = 150, 200, 250, and 300 nm.

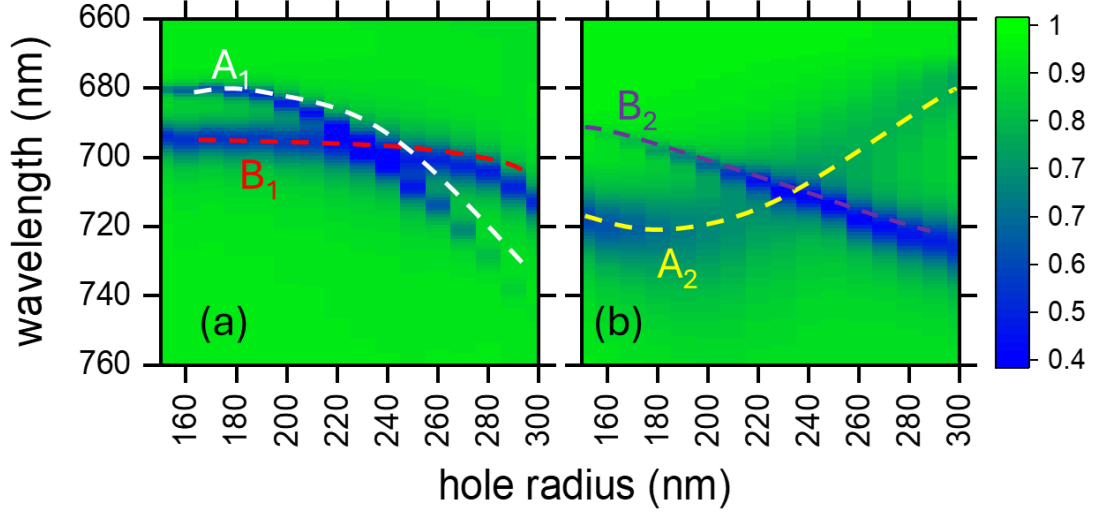


Fig. S8. The (a) p- and (b) s-polarized total reflectivity spectral mappings at the X point for different R. The color dash lines are for the visualization of the A_1 , B_1 , A_2 and B_2 assignments.

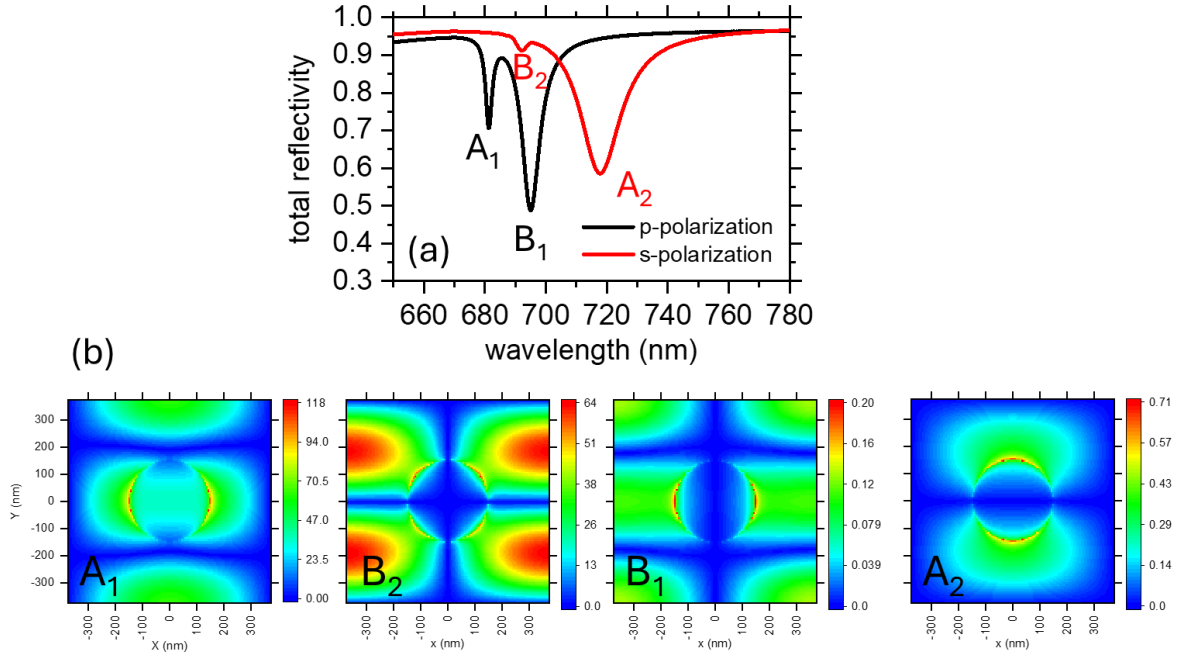


Fig. S9. For R = 150 nm, the (a) p- and s-polarized reflectivity spectra taken at the Γ point. (b) The corresponding field patterns at $\lambda = 680$ (p-excited), 692 (s-excited), 694 (p-excited), and 718 (s-excited) nm and are labelled as A_1 , B_2 , B_1 , and A_2 .

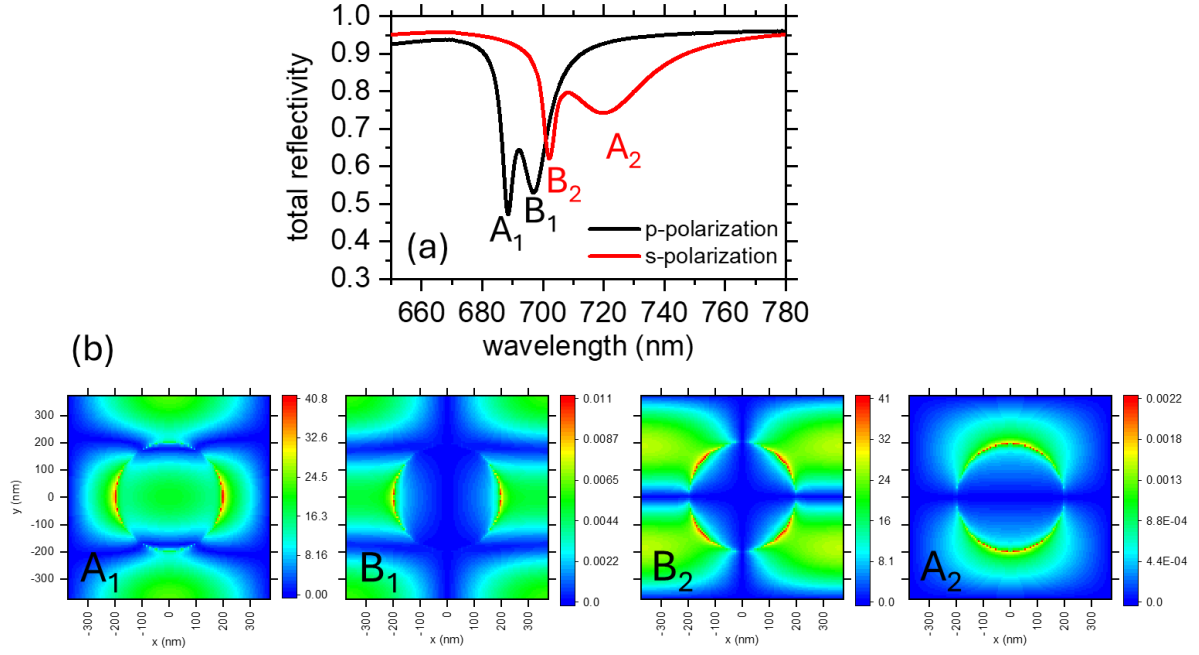


Fig. S10. For $R = 200$ nm, the (a) p- and s-polarized reflectivity spectra taken at the Γ point. (b) The corresponding field patterns at $\lambda = 688$ (p-excited), 697 (p-excited), 702 (s-excited), and 720 (s-excited) nm and are labelled as A_1 , B_1 , B_2 , and A_2 .

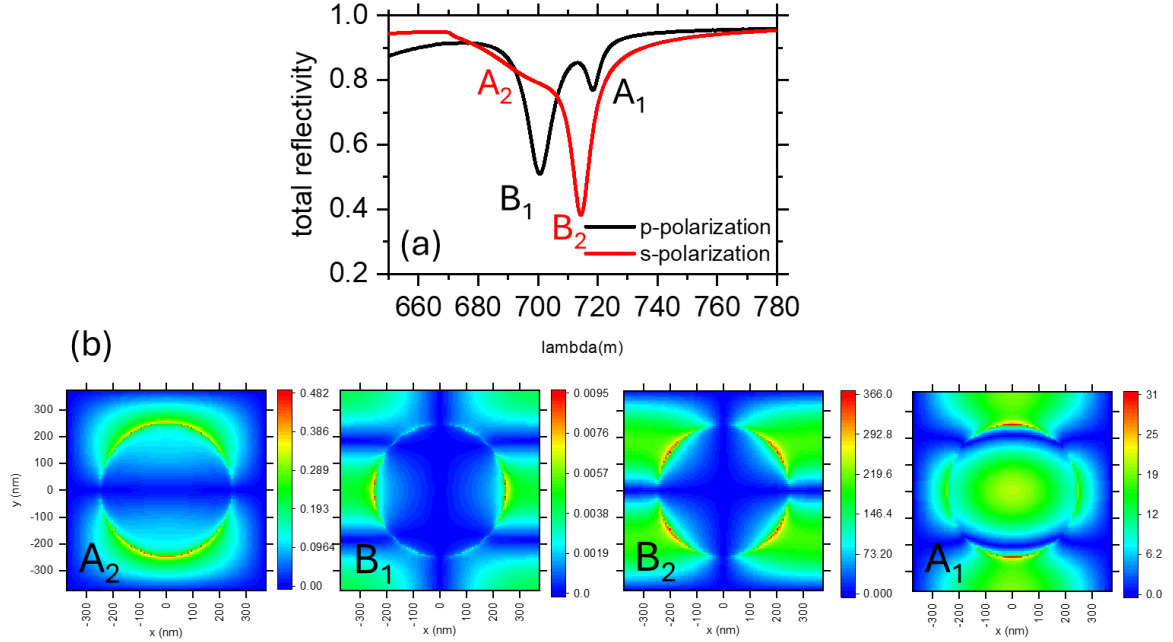


Fig. S11. For $R = 250$ nm, the (a) p- and s-polarized reflectivity spectra taken at the Γ point. (b) The corresponding field patterns at $\lambda = 693$ (s-excited), 701 (p-excited), 714 (s-excited), and 718 (p-excited) and are labelled as A_2 , B_1 , B_2 , and A_1 .

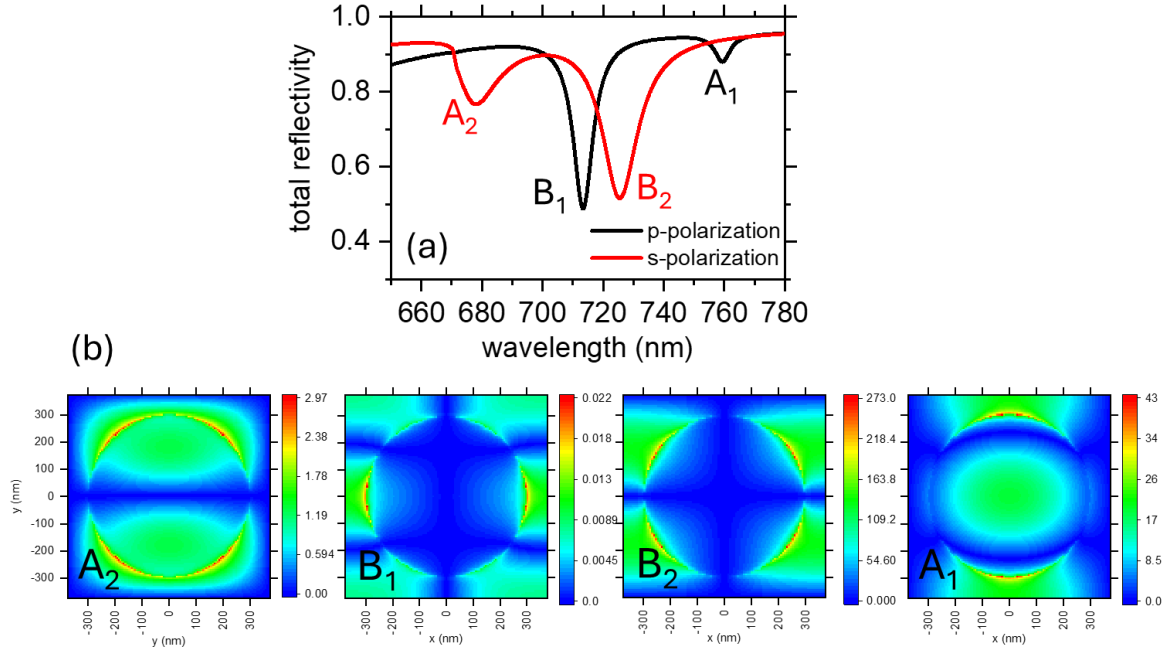


Fig. S12. For $R = 300$ nm, the (a) p- and s-polarized reflectivity spectra taken at the Γ point. (b) The corresponding field patterns at $\lambda = 678$ (s-excited), 713 (p-excited), 725 (s-excited), and 759 (p-excited) and are labelled as A_2 , B_1 , B_2 , and A_1 .

E. FDTD results at the M point

Fig. S13(a) & (b) show the p- and s-polarized radiation spectral mappings taken at the M point for different R. Fig. S14-16(a) & (b) show the field patterns for R = 150, 200, and 250 nm.

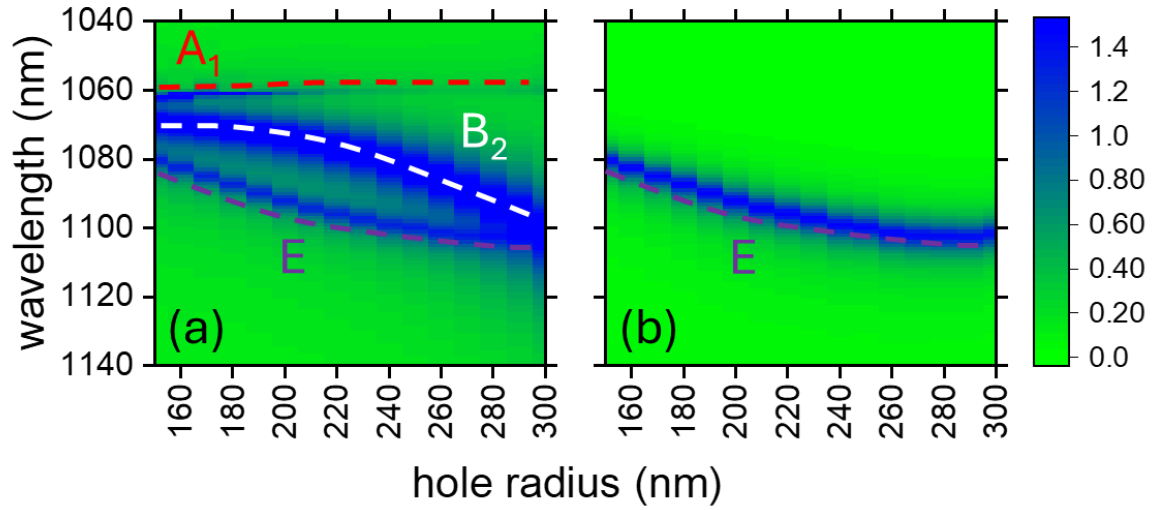


Fig. S13 The (a) p- and (b) s-polarized radiation spectral mappings for different R. The color dash lines are for the visualization of the A₁, B₂, and E assignments.

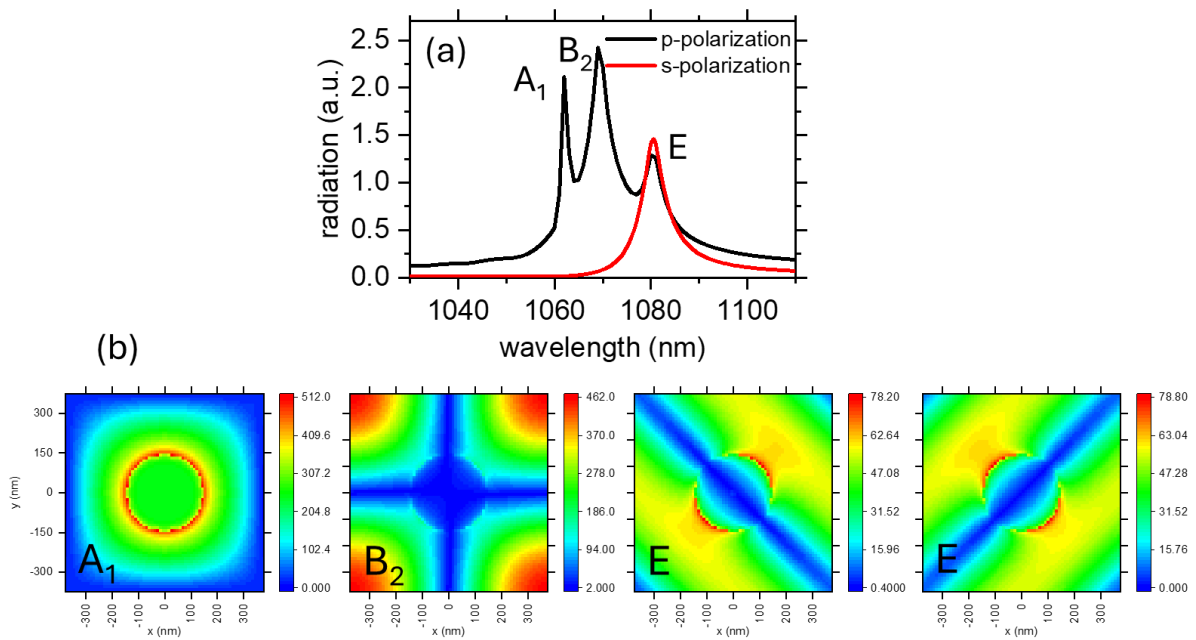


Fig. S14. For R = 150 nm, the (a) p- and (b) s-polarized radiation spectra. The corresponding field patterns at $\lambda = 1062$, 1069, and 1080 nm and are labelled as A₁, B₂, and E.

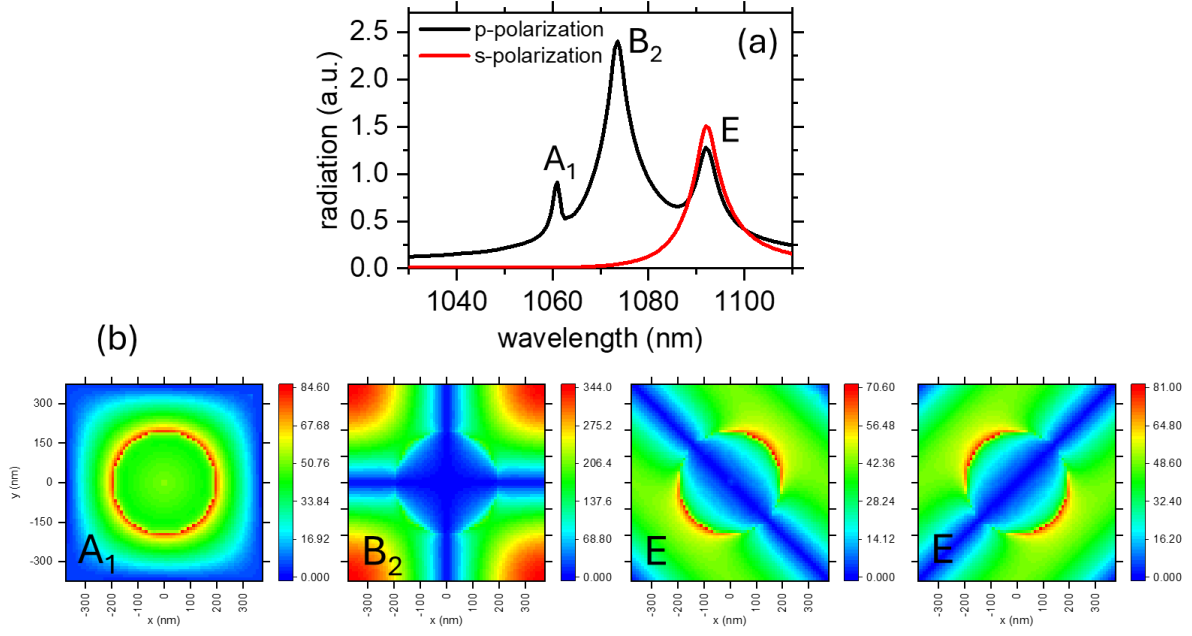


Fig. S15. For $R = 200$ nm, the (a) p- and (b) s-polarized radiation spectra. The corresponding field patterns at $\lambda = 1060$, 1073 , and 1092 nm and are labelled as A_1 , B_2 , and E .

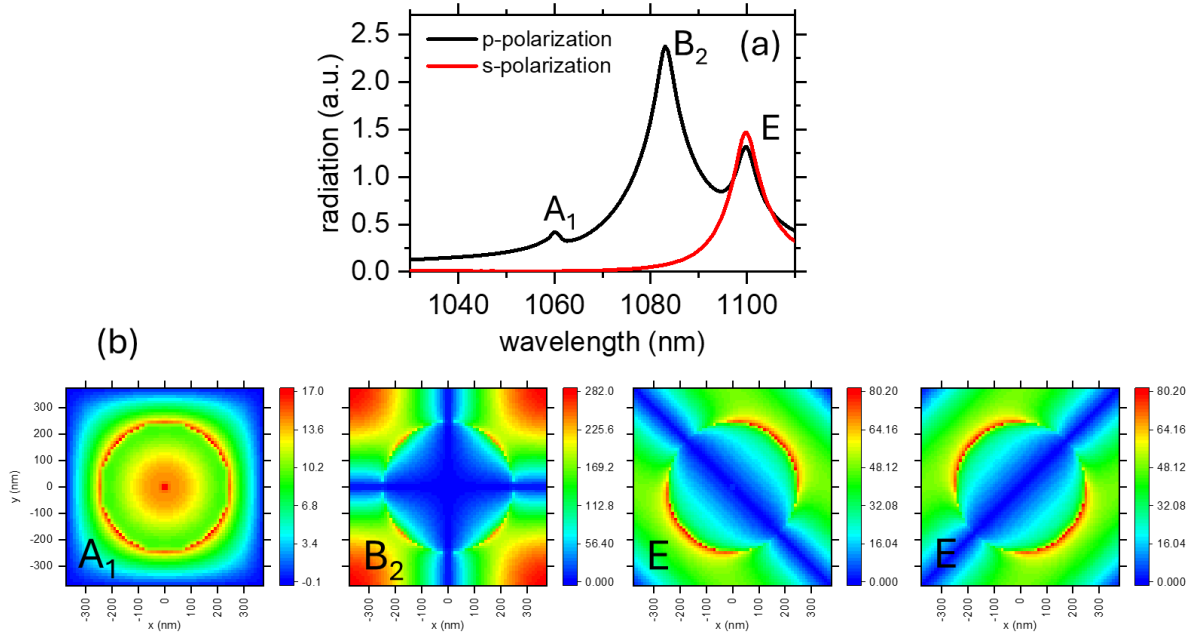


Fig. S16. For $R = 250$ nm, the (a) p- and (b) s-polarized radiation spectra. The corresponding field patterns at $\lambda = 1060$, 1083 , and 1100 nm and are labelled as A_1 , B_2 , and E .

F. Schematic of the Fourier space optical microscope for angle- and wavelength resolved diffraction mapping

Fig. S17 shows the schematic of the Fourier space optical microscope. Briefly, a broadband supercontinuum laser from a nonlinear photonic crystal fiber is collimated and then passed through a set of linear polarizers, wave plates, and lenses before being focused onto the back focal plane (BFP) of a 100X objective lens (OB) with numerical aperture = 0.9. The light exiting from the objective lens is then a collimated beam with well-defined linear polarization. In addition, by displacing the focused spot across the BFP of the objective lens using a motorized translation stage, the incident polar angle θ_i of the collimated beam onto the sample can be varied following $\sin\theta_i = d/f$, where d is the distance between the focused spot and the optical axis of the BFP and f is the focal length of the objective lens. In addition, the azimuth angle ϕ can be varied by a motorized rotation sample stage to align the incident plane to the Γ -X direction of the PmC. The diffractions from the PmC are then collected by the same objective lens and are routed through a set of lens system so that the diffraction orders are projected onto the Fourier space. By placing an aperture at the Fourier space to filter out the desired diffraction order, its intensity and phase spectra can be measured by a spectrometer-based CCD detector.

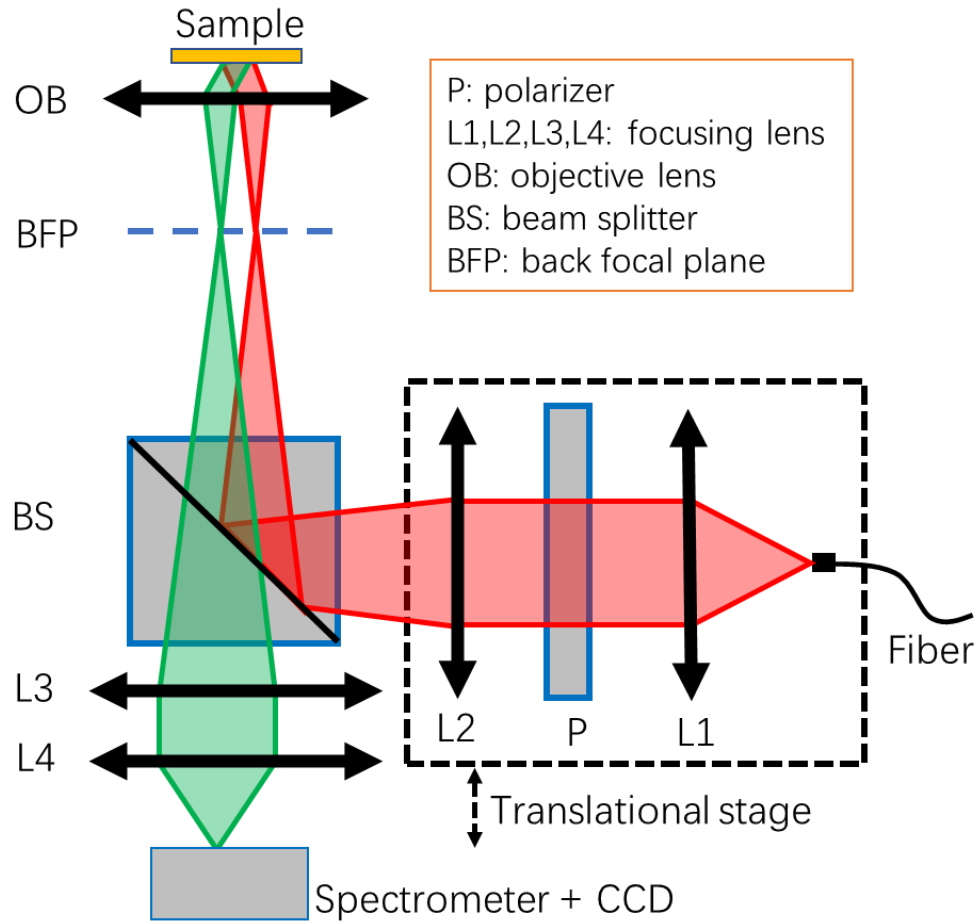


Fig. S17. The schematic of the Fourier optical microscope.

Reference

1. C.M. B. Cordeiro, L. Cescato, A.A. Freschi, and L. Li, Measurement of phase differences between the diffracted orders of deep relief gratings, *Opt. Lett.* 28, 683 (2003).
2. N. Destouches, H. Giovannini, and M. Lequime, Interferometric measurement of the phase of diffracted waves near the plasmon resonances of metallic gratings, *Appl. Opt.* 40, 5575 (2001).